Review Article

Shuxiang Cai, Yalin Sun, Zhen Wang, Wenguang Yang*, Xiangyu Li*, and Haibo Yu

# Mechanisms, influencing factors, and applications of electrohydrodynamic jet printing

https://doi.org/10.1515/ntrev-2021-0073
received July 31, 2021; accepted August 20, 2021

**Abstract:** E-jet printing is a micro- and nano-manufacturing technique that utilizes electric field-induced fluid jet printing for achieving better control and resolution than traditional jet printing processes. In addition to high printing resolution, E-jet printing has advantages in some aspects such as wide material applicability, which has been successfully applied in numerous applications that include sensors, transistors, tissue engineering scaffolds, and photonic devices. This article reviews the electrohydrodynamic jet (E-jet) printing technology, which mainly relies on the principle of electrohydrodynamic-induced fluid movement. At the same time, the process of jet formation and droplet deposition is described. The parameters, nozzle design, and ink characteristics of the jet printing process are summarized. Then, a number of concrete applications based on E-jet printing processes are described in this article. Finally, the future development of this technology has been prospected.

**Keywords:** electrohydrodynamic jet printing, droplet generation process, electronic devices, bioprinting

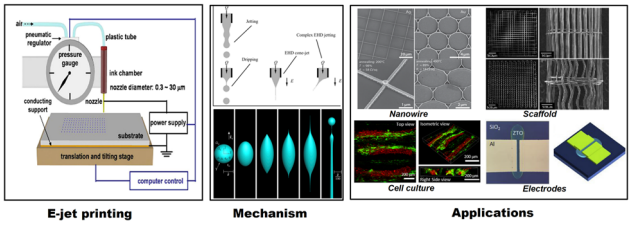


**Graphical abstract**

## 1 Introduction

The technology of fabricating structures at microscale and nanoscale is critical to many existing and emerging industries. The manufacturing of multimaterial and multiscale structures is the current research hotspot of manufacturing science. The photolithography can fabricate microstructures with a size of less than 100 nm and plays a key role in the development of miniaturization and high integration of electronics and semiconductors [1–5]. Moreover, microfabrication/nanofabrication based on photolithography and soft lithography is mainly focused on manufacturing 2D structures, which cannot meet the increasing demand for 3D structures such as flexible electronic devices, stents, and so on.

In contrast, additive manufacturing technology deposits functional materials on the substrate directly, which can achieve precise control point-line-surface step-by-layer manufacturing. As a typical additive manufacturing process, the inkjet printing method can realize the deposition and patterning of functional materials in a drop-on-demand manner. It has attracted great attention in the manufacture of flexible electronic devices since electronic materials provide huge opportunities for the printing technology. Due to its pure additive operation, large-area preparation, low-temperature process, and low cost, inkjet printing has become an effective electronic manufacturing technology to fabricate electronic devices such as transistors, light-emitting diodes, and sensors [6–11]. In addition, inkjet printing is also applied in the fields of optics and biology [12,13]. Thermoelectric or piezoelectric-driven nozzle droplets successfully deposit functional materials on the substrate. Relevant studies have been carried out based on a variety of different materials, from polymers [14], metals or metal oxides [15–18] to various biological materials [19–21]. However, the traditional inkjet printing technology is limited by the size of the inner diameter of the nozzle, and the size of

* **Corresponding author: Wenguang Yang,** School of Electromechanical and Automotive Engineering, Yantai University, Yantai 264005, China, e-mail: ytu_yangwg@163.com
* **Corresponding author: Xiangyu Li,** School of Basic Electrical Engineering, Naval Aviation University, Yantai 264005, China, e-mail: rainlw@126.com
**Shuxiang Cai, Yalin Sun, Zhen Wang:** School of Electromechanical and Automotive Engineering, Yantai University, Yantai 264005, China
**Haibo Yu:** State Key Laboratory of Robotics, Shenyang Institute of Automation, Chinese Academy of Sciences, Shenyang 110016, China; Institutes for Robotics and Intelligent Manufacturing, Chinese Academy of Sciences, Shenyang 110016, China

the droplets produced is usually larger than the inner diameter of the nozzle. Printing smaller droplets requires the design and manufacture of micron-level nozzles. At the same time, small droplets require a greater driving force, and it is difficult to print high-viscosity materials. The existence of these limitations makes inkjet printing difficult to meet the urgent needs of the manufacturing field of micro-nano devices. The resolution and accuracy of microstructures based on laser technology are relatively high, but the process relies on expensive optical systems, and materials are limited to specific photosensitive polymers, which prevents its widespread use. Moreover, compared to conventional fabrication methods such as photolithography, E-jet printing has attractive features including a simple fabrication process, applicability on flexible substrates, compatibility with large-area substrates, and low fabrication cost for printing electronics.

Electrohydrodynamic jet (E-jet) printing, a maskless, noncontact, direct writing, and additive manufacturing process, provides a reliable solution to break the constraints of the aforementioned manufacturing process. E-jet printing technology utilizes an electric field to induce the fluid movement, to stretch ink droplets until the droplets break, and to finally obtain a high-resolution 2D pattern [22–27]. Besides, through layer-by-layer printing, E-jet printing could achieve 3D microstructure/nanostructure fabrication, which provides strong support for the development of the biological field [28–36]. E-jet printing technology maintains the advantages of the traditional inkjet printing technology, such as high flexibility and large area printing. Furthermore, it could achieve high-resolution manufacturing at sub-microscales and can print high-viscosity solutions. Printing accuracy is no longer limited by the inner diameter of the nozzle, and droplets with a size much smaller than the nozzle size could be produced. Therefore, E-jet printing technology has broad application prospects in the future development.

Although the development of E-jet printing has been summarized by other researchers, the theoretical analysis and newly emerging applications are missing. As a consequence, there is an urgent need for a comprehensive and systematic review on this technique. In this article, we mainly review the development of E-jet printing. Section 2 introduces the principle of E-jet printing and some theoretical research carried out by researchers. Section 3 demonstrates three factors that mainly affect E-jet printing: process parameters, nozzle design, and ink characteristics. Section 4 summarizes the application of E-jet printing, from the two aspects of flexible electronic devices and biological application. Section 5 discusses the development prospects of E-jet printing technology.

# 2 The principle and theoretical analysis of E-jet printing

## 2.1 Electrohydrodynamic printing systems

A typical E-jet printing system is composed of a pressure pump, a nozzle, a voltage source, a mobile platform, and a computer control system. The pressure pump pushes the ink to be injected into the nozzle, and the voltage source provides the electric field between the nozzle and the substrate. The system diagram of E-jet printing is shown in Figure 1(a) [37]. Different from traditional inkjet printing, E-jet printing uses a high-voltage electric field to induce the fluid movement instead of squeezing force. When the liquid obtains a sufficient high electric potential, the liquid meniscus forms a stable cone shape, which is called the Taylor cone. The electric field force is used as the driving force to pull the polarized droplet from the tip of the Taylor cone. When the electric field force overcomes the surface tension of the droplet, the droplet is released from the nozzle tip and the size of the ejected droplet is much smaller than the inner diameter of the nozzle. Then, according to the designed pattern, the mobile platform composed of the substrate and the three-axis electric translation stage is moved to deposit the droplets on the specified position accurately, and a large-area droplet array is obtained, as shown in Figure 1(b) [37].

## 2.2 Theoretical analysis of E-jet printing

The dynamic behavior of the electrofluid is affected by the combination of various forces such as liquid pressure, liquid surface tension, and electric field force. The voltage, flow rate, and the properties of ink such as viscosity, conductivity, and surface tension are important factors affecting the formation of jet modes [38–40]. The mechanism of the jet formation process is essential for optimizing electro-jet printing parameters and achieving stable jetting and high resolution. Therefore, before conducting practical operations, it is necessary to establish a mathematical and physical model for the theoretical analysis of the influence of various parameters.

First, jet formation and deposition are of great significance to the resolution and accuracy of jetting. The droplet generation process directly affects the adjustment of process parameters and the performance of the electrofluidic jet printing structure during the preparation of

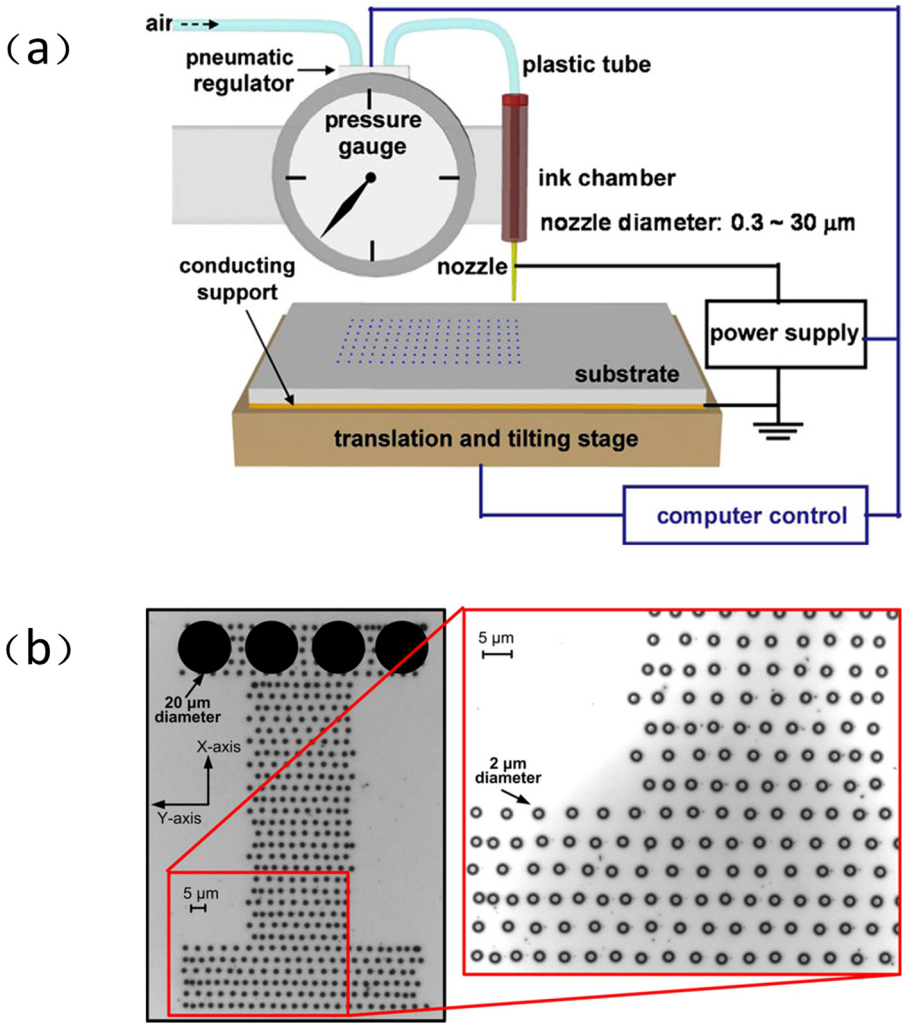


**Figure 1:** (a) The composition diagram of the electrofluidic power jet printing system. (b) A droplet pattern array with an average diameter of 2.8 μm printed by the E-jet printing system. Reproduced from ref. [37] with permission from Elsevier Ltd.

micro-nano-scale functional structures. Simulation of the E-jet printing process is indispensable for the controllability of the system. Collins *et al.* [41] found that the droplet under the action of a strong electric field can produce three different states by changing its conductivity. The deformation of the droplet, the formation of Taylor cones, and the pinch-off state of the droplet are clearly displayed in the simulation, as shown in Figure 2(a) [41]. Pan and Zeng [42] established a physical model based on a variety of coupled physical forces such as electrostatic force, surface tension, hydrodynamic force, viscous force, and gravity, as shown in Figure 2(b) [42]. The whole process of droplet generation in a complete cycle was simulated and experimentally completed, including Taylor cone generation, jet start, jet interruption, and jet contraction. The numerical model is used to further study the effect of three parameters including injection starting voltage, ensuring stable and continuous injection flow rate, and nozzle diameter on printing accuracy. Surface tension and electrostatic force play a key role in the formation of droplets. The relationship between these two forces is helpful to analyze the droplet ejection and deposition. As shown in Figure 2(c) [43], a finite element analysis model of the droplet surface charge and electrostatic field distribution is established [43]. Based on this model, the droplet formation process is analyzed and the relationship between electrostatic force and process parameters is determined. At the same time, the flight speed of the droplet was calculated, and the droplet reached the maximum when it hit the substrate, and then, the deposition of the droplet was simulated. The trajectory of the jetted droplets under the action of an electric field is very important for the precise control of droplet deposition. Wu *et al.* [44,45] analyzed the electric field distribution through a finite

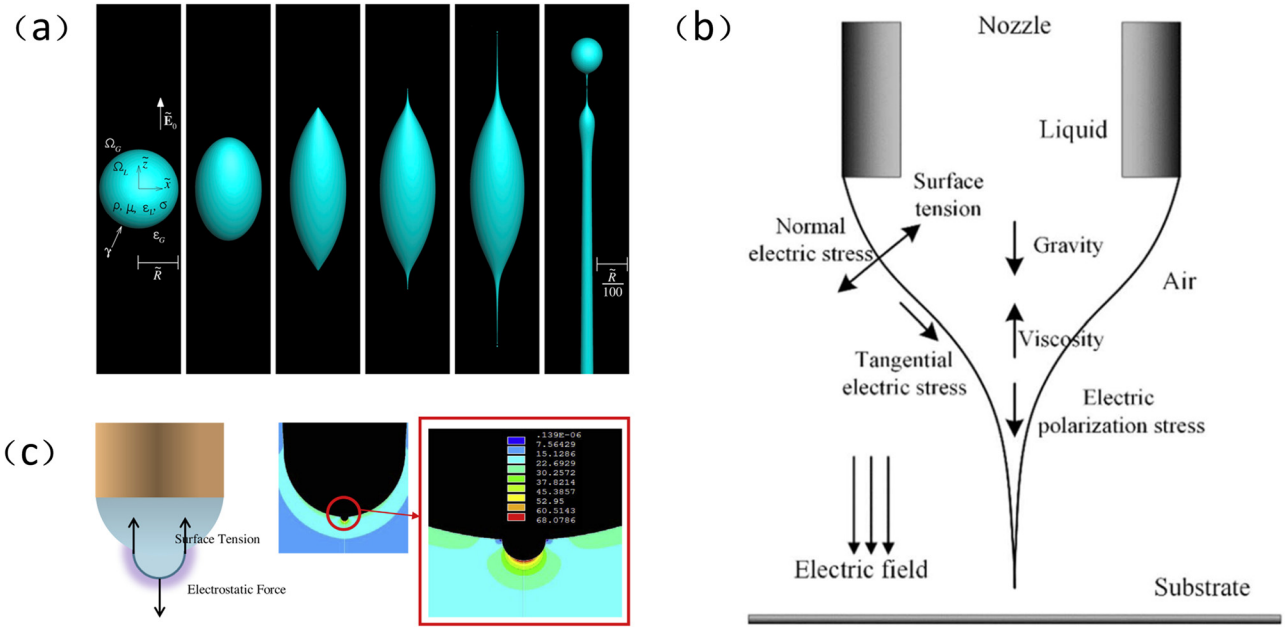


**Figure 2:** (a) The detailed process diagram of the droplet deposition, from the spherical shape to the Taylor cone at both ends and then to the droplet pinching off. Reproduced from ref. [41] with permission from the National Academy of Sciences. (b) Coupling distribution map of various forces of cone jet ejection based on the dielectric model. Reproduced from ref. [42] with a permission from MDPI (Basel, Switzerland). (c) Finite element analysis of the hemispherical meniscus at the tip of the nozzle and the surrounding electric field distribution map. Reproduced from ref. [43] with a permission from Elsevier BV.

element model and found that the electric field intensity at the nozzle tip is the largest. High voltage, low distance between nozzle and substrate, and small nozzle size can enhance the intensity of the electric field. Due to the uneven electric field at the nozzle tip, the direction of the droplets ejected from the edge of the nozzle is deflected; however, the droplets ejected from the center of the nozzle are not deflected.

The jet process of a conventional E-jet system could be calculated using a set of equations in which electrical and mechanical forces are included [46].

$$\frac{\partial \rho_i}{\partial t} + \nabla\cdot(\rho_i v_i) = \sum_{j=1}^{n} I_{ij}, \tag{1}$$

$$\frac{\partial \rho_i v_i}{\partial t} + \nabla\cdot(\rho_i v_i \otimes v_i) = \nabla\cdot\prod_{\ell} + \rho_i g + \sum_{j=1}^{n} P_{ij} + L_\ell. \tag{2}$$

In equation, $i$ refers to gas or liquid phase ($g$ and $\ell$, respectively). The symbol $\otimes$ denotes the dyadic product of the vectors.

The stress tensor on the liquid surface was formularized as follows:

$$\prod_{\ell} = \mathrm{Grad}(lp) + \eta_\ell \nabla v_\ell, \tag{3}$$

where $p$ is the dynamic pressures and $\eta$ is the liquid viscosity. Grad is a difference operator on a scalar, which is due to the pressures on both sides of the interfacial surface ($p_\ell$ and $p_g$):

$$\mathrm{Grad}\, p = p_\ell - p_g. \tag{4}$$

The force density on the liquid jet can be obtained using equations (3) and (4):

$$\frac{\partial \rho_\ell v_\ell}{\partial t} = \rho_\ell g + L_\ell - \phi_{st} - \nabla\cdot(\mathrm{Grad}(lp)) + \eta_\ell \nabla v_\ell + \rho_\ell v_\ell \otimes v_\ell. \tag{5}$$

In addition, during the E-jet printing process, the droplets may be broken down into tiny satellite droplets [47–50], which is undesirable to obtain in the printed pattern because it will affect the resolution of the printing. Therefore, it is very necessary to analyze and study satellite droplets in the process of droplet formation. Huo *et al.* [51] not only discussed the process of droplet formation and the transition of ejection mode but also studied the formation of satellite droplets in the drop mode and whether they aggregate with the main droplet. As shown in Figure 3(a) [51], for low-viscosity liquids, when no electric field is applied, the downward contraction force caused by surface tension ($F_{\sigma 1}$), the upward contraction force caused by surface tension ($F_{\sigma 2}$), and gravity ($F_g$) are three forces that determine the direction of the movement of the droplet. After the electric field is applied, the

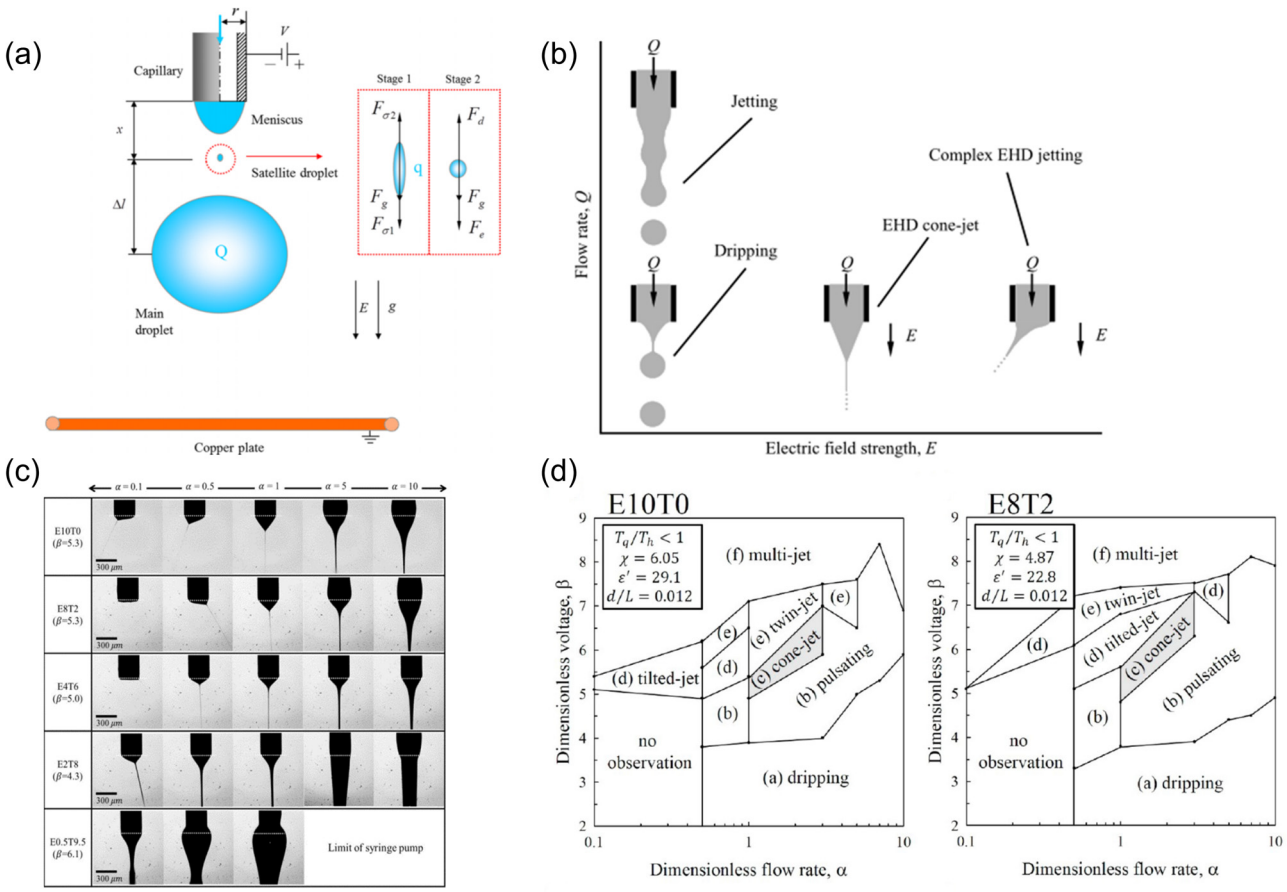


**Figure 3:** (a) Schematic diagram of force action of satellite droplets produced by low-viscosity liquid with or without the electric field. Reproduced from ref. [51] with permission from American Institute of Physics. (b) Several different injection modes as the electric field and flow rate change. Reproduced from ref. [53] with permission from Cambridge University Press. (c) Changing the nondimensional parameters of flow rate $\alpha$ and voltage $\beta$ changes in injection behavior. (d) Four mixed ink (E10T0, E8T2, E4T6, and E2T8) jet behavior diagrams drawn according to flow rate $\alpha$ and voltage $\beta$. Reproduced from ref. [60] with permission from American Chemical Society.

electric power ($F_d$) from the charged main drop and the Coulomb repulsive force ($F_e$) from the electric field between the electrodes dominate. This study shows that when the number of electronic bonds is low, the satellite droplets move upward until they gather with the meniscus, and when the number of electronic bonds is high enough, the satellite droplets will reciprocate up and down between the two meniscuses. Guo *et al.* [52] used numerical simulation methods to study the generation and ejection behavior of satellite droplets because the charge relaxation time determines the electrical repulsion between the satellite droplet and the meniscus. The charge relaxation time is used to study whether the satellite droplet will merge or separate with the meniscus. Results have shown that a longer charge relaxation time will help the satellite droplets merge with the meniscus, while a too short charge relaxation time will cause the satellite droplets to fall. At the same time, the dielectric constant and flow affect the charge relaxation time.

Second, due to the interaction of various factors during the E-jet printing process, different jetting modes are formed. As Collins *et al.* [53] and Jaworek and Krupa [54] summarized in their article, the injection modes include drip mode, pulsation mode, stable cone injection mode, and complex injection modes, such as oblique injection, double injection, and multiple injection, as shown in Figure 3(b) [53]. In the case of low electric field strength and low flow rate, the electrostatic force produced by the electric field offsets the surface tension, and the droplets are clamped off from the nozzle under the action of gravity to produce dripping. Before the flow rate increases to the minimum flow rate that can produce a stable cone jet mode, the nozzle presents a hemispherical or Taylor conical meniscus. Unlike the dripping mode, this pulsed jet mode does not shrink the meniscus after the droplets are separated. The dripping and pulsating modes can be produced only within a limited flow

rate and voltage range. When the voltage exceeds a certain critical value, the electric field forces the droplets to cause a spindle shape. This mode is called the spindle mode. When the voltage value increases to the critical voltage, a stable cone jet pattern is generated, the liquid forms a regular Taylor cone at the nozzle, and the jet is ejected symmetrically along the axis. A further increase in the electric field leads to an imbalance between the various forces, thus producing oblique jets. The voltage value continues to increase, and multiple jets will be generated from the meniscus, resulting in dual jets or even multiple jets. Among them, the pulsating jet mode and the stable cone jet mode are essential for depositing functional materials on the substrate to obtain high-resolution micro-nano structures.

There have been many studies on the ejection mode and droplet formation process of E-jet printing. For pulsating ejection and cone ejection modes, various scaling laws [55–58] for the influence of various parameters such as voltage intensity, flow rate, and conductivity on the size of the droplet has been proposed. Hartman *et al.* [55] first proposed a model that can calculate the shape of the liquid cone and jet, and electric field strength, charge density, and current passing through the cone. The error between the experimental result and the simulating result is within 10%, which provides a theoretical foundation for subsequent research. Scheideler and Chen [59] studied the scaling law for controlling the minimum flow rate of a stable Taylor cone jet ejected from a charged nozzle. At low viscosity, the minimum flow rate does not depend on the nozzle diameter, but strongly depends on the conductivity of ink. In contrast, the minimum flow rate of a high-viscosity liquid is basically independent of the conductivity of the liquid, but strongly depends on the nozzle diameter. Most of the previous studies only analyzed the cone jet from a single aspect of material properties or printing parameters. It is necessary to study the effect by combination of these two aspects of the system. Therefore, Lee *et al.* [60] systematically analyzed the influence of processing parameters and ink characteristics on obtaining a stable Taylor cone jet pattern.

During the printing process, the charges move toward the surface and cause the electric normal stress [$\tau_{E,n}$]. The charge conduction was influenced by the supplied flow rate $Q_s$ (related to the resistance, $\sim K^{-1}$) and electrical charging time (related to the capacitance, $\sim\varepsilon_0\varepsilon'$). The surface charges induced by charge conduction lead to electric tangential stress along the surface meniscus with acceleration toward the cone apex. A jet is formed by these charge and fluid motions. Electric field ($E = V_a/L$), the charge amount ($\varepsilon'$), and the flow resistance ($\eta$) are the variables influencing the charge convection. Therefore, there are 10 variables determining the electrodynamics and fluid dynamics for E-jet printing: $\rho$, $\gamma$, $\varepsilon_0$, $\varepsilon'$, $K$, $\eta$, $d$, $L$, $Q_s$, and $V_a$. Then six dimensionless numbers $D_1$–$D_6$ are designed to systematize the 10 influencing variables. These dimensionless numbers are respectively related to processing time ($D_1$), material properties ($D_2$ and $D_3$), geometry ($D_4$), and processing conditions ($D_5$ and $D_6$). The cone jet is produced in the balance of flow and electric field intensity. The mixtures of ethanol and terpineol were injected using different proportions. Figure 3(c) [60] shows the injection behavior corresponding to different flow rates and voltages. According to the classical injection mode, the injection diagrams between different flow rates and voltages under different material properties are drawn, as shown in Figure 3(d) [60]. To obtain a stable cone jet, the ratio of the electric normal force to the electric tangential force on the surface of the Taylor cone is proposed as a parameter to evaluate the degree of stability. The value becomes smaller and the stability increases. In the case of the inherent pulsation of the liquid jet, the proportional relationship related to the jet diameter is proposed [57]. The jet diameter is proportional to the square root of the nozzle size and inversely proportional to the electric field strength, which provides a theoretical basis for the study of the influence factors of the jet process. From the theoretical analysis, Lee *et al.* [61] obtained the model of the initial voltage for the transition from the drip mode to the pulsation state, the threshold voltage for the transition from the pulsation mode to the stable cone jet mode, and the relationship between the droplet diameter and the voltage. At the same time, the jet state of four different surface-active waters before and after reaching the initial voltage was studied. Among them, the stability of the pulsating drop of cations was the best.

# 3 Influencing factors of E-jet printing

The droplet ejection process is affected by many factors, such as ink properties (viscosity, conductivity, surface tension), process parameters (applied voltage, flow rate), and nozzle structure (nozzle diameter and nozzle design; Table 1). These influencing factors as the input of the system play a vital role in the output (droplet size, ejection speed) of the E-jet printing system. Recently, Mohammadi *et al.* [62] through numerical simulation analysis found that the dielectric constant, conductivity, flow rate, voltage, viscosity, and

**Table 1:** Influencing factors of E-jet printing

| Influencing factors of E-jet printing | Results of influence |
|---|---|
| Process parameters | |
| Electric field strength | Increasing the voltage will reduce the droplet size |
| Moving speed of nozzle | The line width and the line height did not change significantly |
| The distance between the nozzle and the substrate | As the distance increases, liquid jet on the substrate become viscous |
| Nozzle design | |
| Structure | The meniscus formed at the end of a hypodermic needle is much smaller and the nonconductive tip help form a stable jet |
| Multi-nozzles | The high production rate |
| Ink characteristics | |
| Surface tension | The pulse duration decreases with increasing surface tension |
| Density | Larger particles in the ink will lead to the formation of satellite droplets |
| Viscosity | The printing jet volume increases with the increase of viscosity |
| Conductivity | The printing jet volume decreases with the increase of conductivity |

nozzle diameter have a greater influence on the diameter of the droplet. The speed of the droplet produced is mainly affected by the voltage, the distance between the nozzle and the substrate, and the conductivity. The three parameters of viscosity, voltage, and dielectric constant are related to the breaking distance of droplets. Among all input parameters, voltage, dielectric constant, nozzle height above the substrate, viscosity, and conductivity are the most effective parameters for process output.

## 3.1 Process parameters

E-jet printing is the result of the coupling of various forces such as electrostatic force and surface tension. To obtain a stable printing process and high-resolution printing results, it is necessary to adjust and optimize the process parameters, such as electric field strength, flow rate, the distance between the nozzle and the substrate, and the moving speed of the mobile stage. Among many factors, the applied voltage is the main factor. Generally, increasing the voltage will reduce the droplet size (better resolution) and increase the ejection frequency of the droplets because the higher voltage and the electric field strength increase the surface charge density at the Taylor cone. Therefore, a small droplet can obtain a large enough electrostatic force to overcome the surface tension, so as to be ejected from the tip of the cone. The high electric field also increases the rate of surface charge accumulation. Therefore, the frequency of droplet formation and ejection also increases. For example, Han *et al.* [63] increased the voltage value from 850 to 1,000 V. Correspondingly, the droplet size was reduced from 15 to 7 μm, and the printing speed was increased from 6 to 22 Hz. Wei and Dong [64] studied the effects of voltage, plotting speed, and pressure on the stable electrohydrodynamic cone jet mode. As shown in Figure 4(a) [64], low voltage, higher plotting speed, and higher pressure result in a skewed cone jet. The larger electrostatic stress caused by the large voltage and small pressure indicates a larger jetting speed. Therefore, it is very important to match the jetting speed and the plotting speed. When the jetting speed is lower than the plotting speed of the platform, the skewed cone jet is produced. When the jetting speed matches the plotting speed, a straight cone jet is obtained. When the jetting speed is higher than the plotting speed, wavy filaments are produced due to the speed mismatch. However, if the applied driving voltage is higher than the threshold voltage, electrical breakdown may even occur. According to reports, after the start of the jet, the driving voltage is gradually reduced, and the jet can still be jeted continuously, depending on the molecular weight ($M_v$) and weight percentage (wt%) of the solution [65]. Jang *et al.* [65] studied the ejection behavior through the relationship between the ratio $R$ of the driving voltage $V_d$ and the threshold voltage $V_{th}$, $M_v$, and wt%. The jet behavior of different solutions is similar under high $R$ value, and the value of $M_v$ and wt% should be increased to obtain a thinner jet under low $R$ value. The low $R$ value causes the solvent of the jet to evaporate before reaching the substrate, and solid fibers are formed on the substrate. Changing the polymer weight percentage, molecular weight, and voltage drop rate leads to the transition of the jet mode. At high concentrations, the $R$ value is reduced, and the transition from micropatterns to nanopatterns to nanofibers can be realized, and low-voltage driving high-resolution pattern printing can be achieved.

The E-jet printing process has great potential in manufacturing 3D microstructures [66–69]. The line width

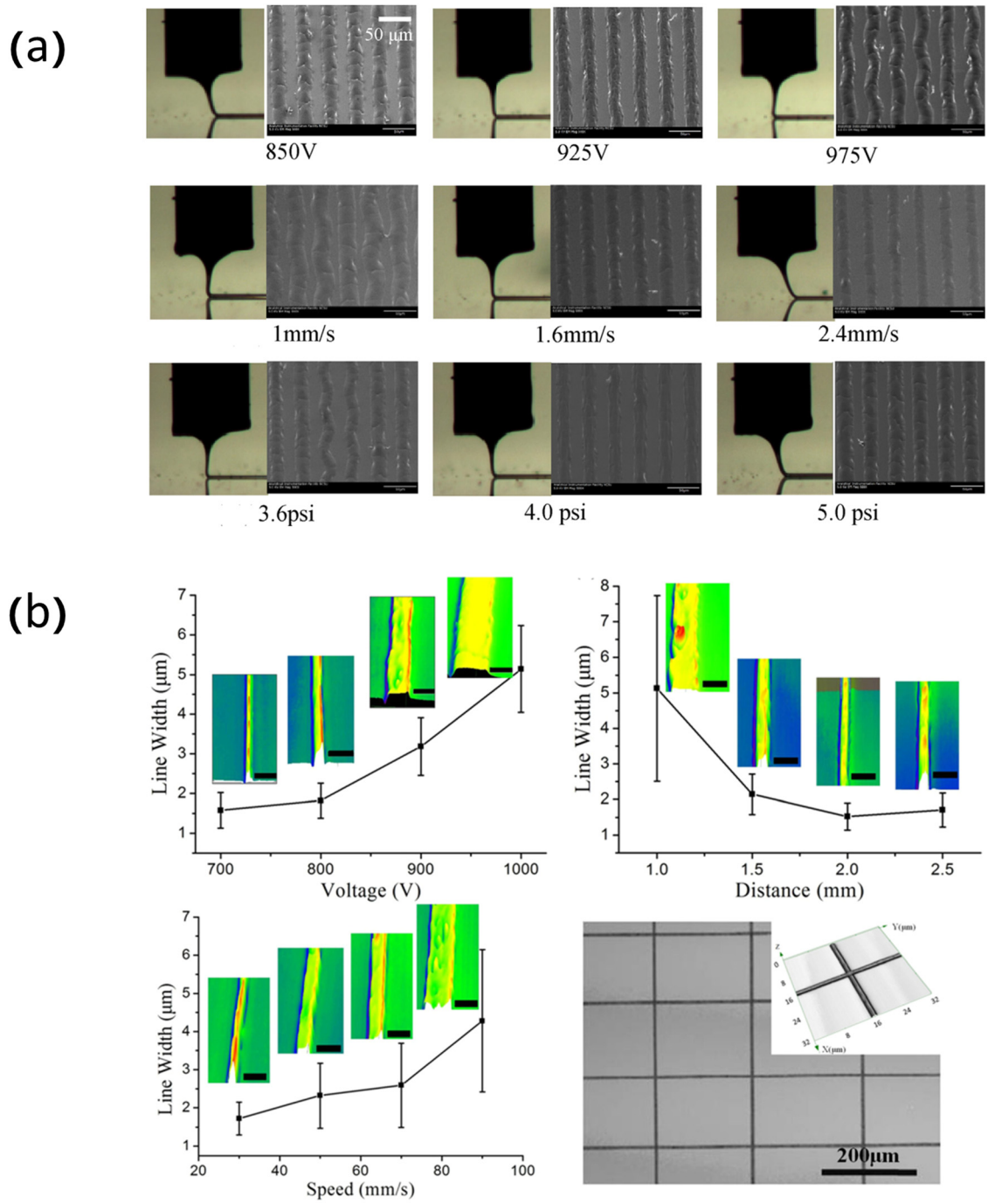


**Figure 4:** (a) The cone jet shapes and jet filaments under different voltages, plotting speeds, and pressures. Reproduced from ref. [64] with permission from Elsevier BV. (b) The effect of changing the applied voltage, the distance from the nozzle to the substrate, and the moving speed of the nozzle on the line width of E-jet printing. Reproduced from ref. [72] with permission from American Institute of Physics.

and the shape of the 3D pattern are significantly affected by the operating parameters. In previous studies, the structure shape was affected by the moving speed of the collector [70,71]. While the electro-hydrodynamic direct writing proposed by He *et al.* [72] designed the nozzle as a moving part, the line width and the line height did not change significantly for different nozzle speeds. As the applied voltage increases, the line width increases and the printing height decreases. As the distance from the nozzle to the substrate increases, the water fully evaporates during the printing process, causing the liquid jet on the substrate to become viscous and the diffusion effect is

reduced, so the line width becomes smaller and the line height increases. The printing results of changing different parameters are shown in Figure 4(b) [72]. Zhang *et al.* [69] proposed a hybrid mechanism composed of E-jet printing and fused deposition modeling technology, which optimizes and adjusts the printing parameters comprehensively in terms of nozzle size, voltage, printing speed, temperature, and feed speed. The results show the limitations of printing with large nozzles. When certain conditions are reached, large nozzles make the ejection behavior unstable. Temperature affects the viscosity of the printing material, which in turn affects the line width. In a certain temperature range, the line width decreases when the temperature rises. Finally, a eight-layer 3D stent with a resolution of 10 μm was printed under the best conditions of a nozzle inner diameter of 200 μm, a temperature of 240°C, a voltage of 1 kV, and a printing speed of 35 mm/s. Similarly, He *et al.* [68] achieved the layer-by-layer printing line by optimizing the voltage and the moving speed parameters of the collector under 800 V and 20 mm/s. The average thickness of the printed wall below 100 layers is about 0.71 μm. Due to the change of the electric field between the nozzle and the substrate, as the number of layers increases, the average thickness increases. If the number of layers is too high, the printed structure will deform in the vertical direction. Therefore, the maximum height of the multilayer 3D structure printing is often limited by the distance between the nozzle and the substrate. If 3D microstructures are to be stacked layer by layer, the distance between the nozzle and the substrate must be changed accordingly [73].

Liquid deposition rate and liquid size are output parameters affected by input parameters and are also the most important parts of a system. Researchers analyze and describe the printing results from different process parameters [74–76]. Yuan *et al.* [77] proposed a method of using low conductivity to generate adjustable pulsating cone jets. The entire cone jet is divided into three stages: liquid accumulation, Taylor cone formation, and multiple emissions. The Taylor cone formation time is significantly affected by the voltage frequency. Due to the large nonelectrical time at low voltage frequencies, the Taylor cone formation time changes little at frequencies below 30 Hz. The deposition frequency in a cycle decreases as the voltage frequency increases, and the flow rate has only a slight effect. At the same time, the droplet size also decreases with the increase of the voltage frequency. But using a large flow and sufficient liquid supply can compensate for the liquid loss after launching and slow down the rate of decrease. A stable deposition process requires a low-frequency voltage, and precise control of the generated droplets can be achieved by selecting a high-frequency voltage and a large flow rate. Han and Dong [78] studied high-resolution E-jet printing based on molten metal jetting. They characterized the impact of electrostatic field and printing speed on the printing process. This system could produce discontinuous metal lines using a voltage of 1,000 V. Meanwhile, if the voltage increased to 1,500 V, a continuous thin wire with a diameter of about 40 μm is obtained. Printing speeds that are too fast or too slow will also cause discontinuous structures. At a printing speed of 3–5 mm/s, fine metal wires can be printed. The jet breaking before reaching the substrate seriously affects the quality of the pattern. Because the cone length and jet length are affected by the intensity of the electric field, they decrease as the voltage increases. As the nozzle size decreases or the flow rate increases, the starting voltage to form the cone jet also increases, so the length of the cone and jet decrease, as shown in Figure 5(a) [79]. Therefore, to improve the printing quality to obtain a small line width and avoid spray deposition due to jet breakage, Park *et al.* [79] set the distance between the nozzle and the substrate to be less than the sum of the cone and the jet length under the conditions of a given voltage, nozzle size, and flow rate. As shown in Figure 5(b) [79], the line width of 32 μm is obtained at the distance from the nozzle to the substrate of 0.8 mm. The small nozzle-to-substrate distance and the nozzle diameter do not affect the spray size, and the increase of the nozzle-to-substrate distance leads to the appearance of satellite droplets. The relationship between the various process parameters plays an important role in determining the size of the printed droplets. Hassan Saba *et al.* [80] established mathematical models among various process parameters through five steps: charge transfer time and ink transfer time, minimum voltage generated by droplets, pulse frequency, duty cycle, and speed of the mobile station. Based on these mathematical models, to obtain a droplet with a diameter of 140 μm, a voltage of 2.5 kV, a pulse frequency of 20 joints, a duty cycle of 41.3%, and an XY stage speed of 6 mm/s were determined.

To obtain better printing performance, it is necessary to adjust and improve the printing parameters. Usually, a DC voltage is applied to an E-jet printing system, which has limitations in controllability. Due to the coupling of process conditions, it is difficult to control droplet size and printing rate separately. The jet of E-jet printing can naturally generate a pulsed flow, and the frequency of the jet and the size of the generated droplets can be regulated by changing the voltage [56]. High-frequency and small droplets require a sufficiently large voltage difference.

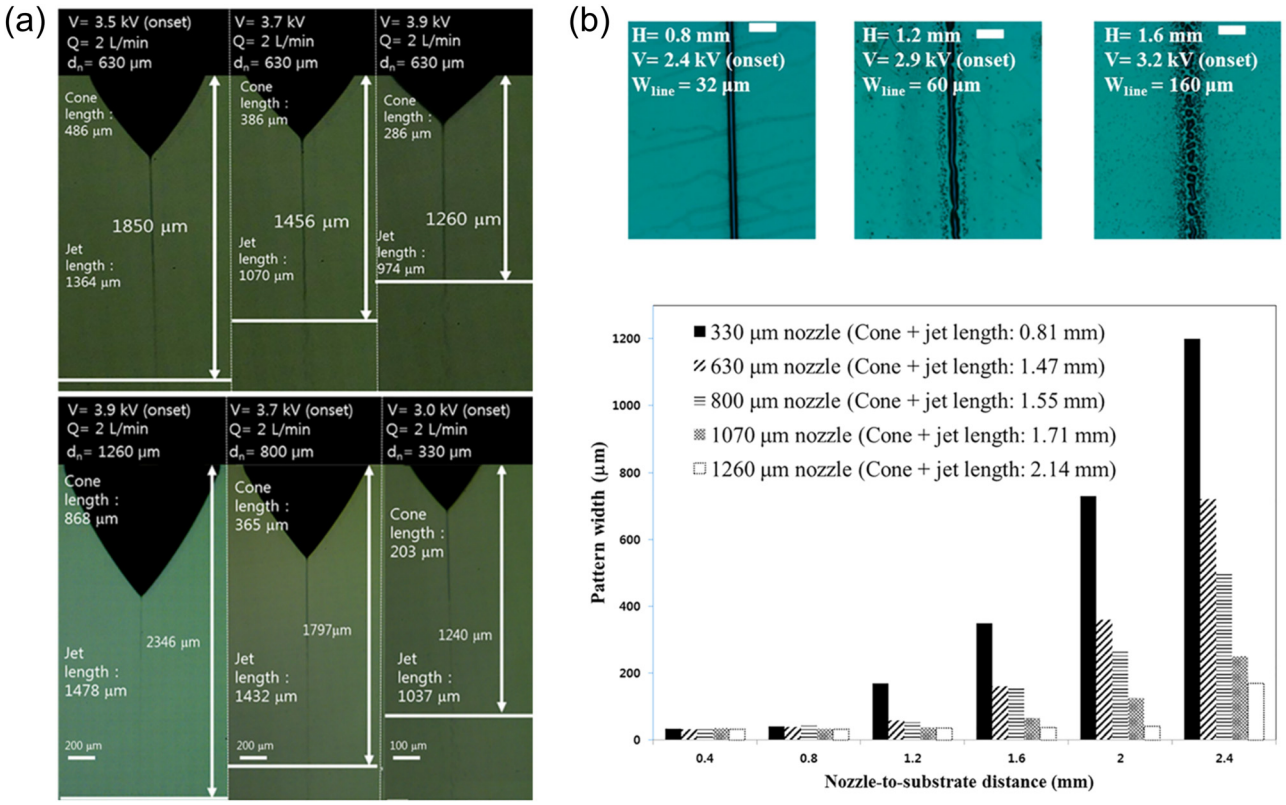


**Figure 5:** (a) Cone and jet length change graph for different voltages, nozzle sizes and flow rates. (b) Line images of different nozzle to substrate distances. Reproduced from ref. [79] with permission from American Institute of Physics.

Under strong electric field conditions, the distance between the nozzle and the substrate is more likely to change in these process conditions, and the ejection frequency will change significantly, resulting in inconsistent gaps between the print droplets. Natural pulse jetting is not suitable for printing patterns with regular droplet gaps and consistent droplet sizes [81]. An E-jet printing system driven by pulse voltage was proposed by researchers [81–84] to overcome these limitations and realize the controllability of jetting. The controllability of the printing speed is related to the pulse voltage frequency. As shown in Figure 6(a) [82], the droplet generation frequency is almost the same as the pulse voltage frequency, and there is a one-to-one correspondence between the two. The pulse duration is less than the Taylor cone formation time, and ejection does not occur. Therefore, the limiting frequency of droplet generation is determined by the formation time of the Taylor cone. By adjusting different voltage frequencies, periodic pulse cone jets produce uniformly arranged droplet arrays with a size controlled between 95 and 210 µm [82]. As shown in Figure 6(b) [82], the droplet size decreases with the increase of the pulse voltage frequency. Rahman *et al.* [85] proposed an on-demand E-jet printing technology using multilevel pulse voltage. The multilevel voltage is composed of a lower limit voltage $V_a$, an intermediate voltage $V_b$, and an upper limit voltage $V_c$ for stable cone pulse injection. They have the same frequency but different duty ratios. Compared with the square wave pulse voltage, the multistep pulse voltage has an intermediate voltage, which avoids the meniscus disturbance and ejection instability caused by the sudden application of high pulses. The multilevel voltage amplitude and frequency have an effect on the droplet diameter. The droplet size obtained at a frequency of 325 Hz is approximately 40 µm. Due to the limitation of lower pulsation frequency [82,83,85], a high-speed on-demand electro-injection method using pulsed DC voltage signals is proposed [81]. High-pressure jet printing has limitations for droplets with the same size, and low-pressure E-jet printing has a slow printing speed. This method superimposes a high-voltage pulse to eject droplets on the basis of the reference voltage. The choice of the reference voltage is critical, but it must be sufficient to form and maintain the Taylor cone. The pulse E-jet printing achieves a printing speed of 1 kHz. Independent control of droplet size and droplet spacing is achieved by regulating the pulse duration and the time interval

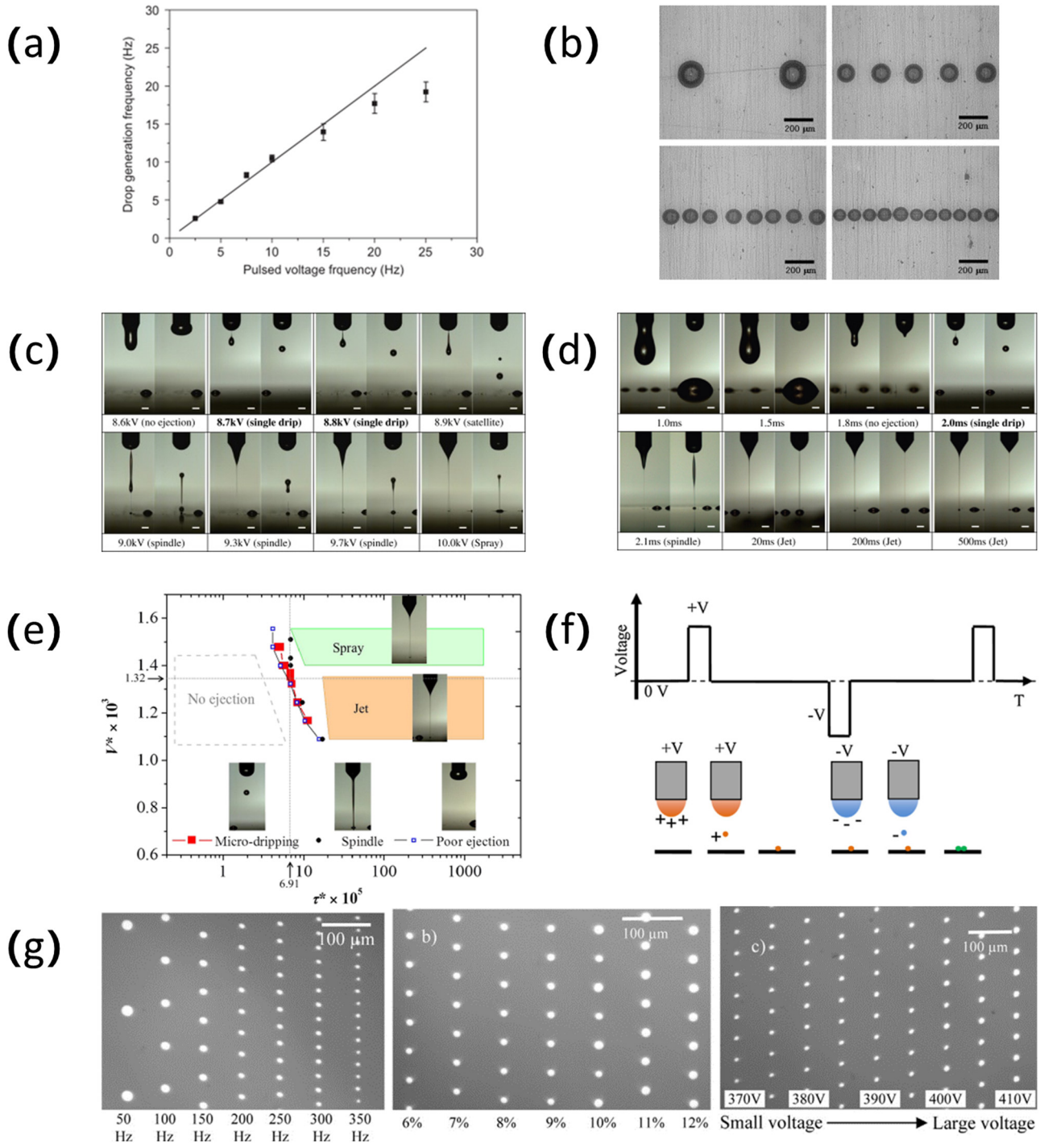


**Figure 6:** (a) Graph of the relationship between droplet deposition frequency and pulse voltage frequency. (b) From top to bottom, from left to right, droplet deposition patterns with pulse voltage frequencies of 2.5, 7.5, 15, and 25 Hz. Reproduced from ref. [82] with permission from Elsevier Ltd. (c) The effect of voltage amplitude on injection mode. (d) The effect of pulse duration on injection pattern. (e) The state diagram of the injection mode based on the dimensionless duration and voltage. Reproduced from ref. [84] with permission from Elsevier Ltd. (f) Typical AC pulse voltage waveform diagram for E-jet printing. (g) The influence of AC pulse frequency, duty cycle, and voltage on droplet size. Reproduced from ref. [92] with permission from Elsevier.

between two consecutive pulses. The droplet size is achieved by repeated adjustments of experimental parameters. The dimensional controllability depends on parameters such as applied voltage, flow rate, surface wettability, and frequency. However, repeated experiments require a lot of time and cost. Park *et al.* [86] proposed two mathematical

models to predict the size of points and lines. For a pattern with a certain size, according to the relationship between the size and the various process parameters in the proposed mathematical model, the required experimental conditions can be obtained, such as flow rate, frequency, duty cycle, and stage speed. When the applied voltage amplitude and pulse duration are changed, the ejection mode of the droplets is significantly different. Lee *et al.* [84] studied the ejection mode of droplets under different parameters and the pulse voltage amplitude and duration increase respectively, as shown in Figure 6(c) and (d) [84]. It is determined that the best pulse injection mode can be achieved when the duration is 2 ms and the voltage is between 8.7 and 8.8 kV. Finally, a dimensionless graph of pulse duration and amplitude is drawn according to the data. As shown in Figure 6(e) [84], the ranges of the four jet modes of pulsation mode, spindle mode, jet mode, and spray mode are determined.

Another challenge of E-jet printing based on the traditional DC voltage is that due to the existence of residual charges of the droplets, the distribution of the electrostatic field and subsequent changes in the printing behavior are caused. Especially on highly insulated substrates, the charge decay rate is very slow. When the droplets are sprayed on the insulating substrate, the charge will be stored for a long time, causing the Coulomb repulsion between the droplets on the substrate and the spray jet, which will cause the jet path to change [87–89]. The residual charge makes E-jet printing a challenge for printing high-resolution continuous structures. To minimize the effect of residual charge, AC pulse voltage is used in the E-jet printing process [90–92]. Park and Hwang [90] used AC-based jet printing for the first time to prepare a silver grid network on a polyethylene terephthalate substrate. Using sinusoidal AC pulse voltage to drive the jet, each positive and negative pulse will produce one jet, and the positive and negative charges will be jetted alternately, so the charged droplets are neutralized and will not cause the droplets and jets to repel. Under the conditions of a fixed flow rate of 0.1 μL/min, a voltage with a peak-to-peak value of 1.4 kV and a frequency of 2 kHz, the speed of the translation stage was adjusted to finally obtain a silver grid network with a line width of 13 μm and a line spacing of 250 μm. Wei *et al.* [92] proposed a method of using AC pulse voltage to achieve continuous printing on highly insulating substrates. The AC pulse waveform diagram is shown in Figure 6(f) [92]. By adjusting the three process parameters, pulse frequency, pulse voltage amplitude, and duty cycle, independent control of droplet size and printing frequency is achieved. Among them, the pulse frequency is used to control the printing frequency, and the voltage amplitude and duty cycle determine the droplet size. Figure 6(g) [92] shows the experimental results of adjusting the three parameters to print droplets. Low-frequency pulses, large duty cycles, and high voltage amplitudes produce large droplets. Qin *et al.* [93] achieved 5.9 μm single-layer silver trace printing under the conditions of applying an AC pulse voltage of 400 V, a frequency of 1,000 Hz, and a duty cycle of 10%. The silver traces with an average line width of 13.1 μm were printed by stacking layers of droplets layer by layer.

## 3.2 Nozzle design

As an important part of the E-jet printing system, the nozzle is not only the outlet of the liquid jet but also considered as an electrode. The size and structure of the nozzle is one of the main factors that affect the resolution of the droplets. To obtain a stable jet and higher resolution, optimal design of the nozzle is necessary [94–97]. Kim *et al.* [98] compared the effects of two different shapes of jetting needles on the resolution of printed patterns. As shown in Figure 7(a) [98], a flat needle with an inner diameter of 100 μm and a hypodermic needle are used. The hypodermic needle is more hydrophilic after being irradiated with ultraviolet rays. Compared with a flat needle that produces a large meniscus, the meniscus formed at the end of a hypodermic needle is much smaller. Figure 7(b) [98] shows that the flat needle has a line width of 59 μm, which is about 59% of the needle diameter, while the line width of the hypodermic needle reaches 0.7 μm, which is only less than 1% of the needle diameter. Kim *et al.* [99] developed a capillary nozzle with a nonconductive tip. Compared with common nozzles, a nonconductive tip nozzle requires a smaller voltage value to obtain a stable cone jet, and a pattern size of 30–62 μm can be obtained. The nonconductive tip will help reduce the set voltage by reducing the backflow near the tip of the liquid flow, thereby helping to form a stable jet. Recently, a novel nozzle tip-assisted E-jet printing method was proposed, as shown in Figure 7(c) [100]. This method inserts a tip with a diameter of 20 μm and a height of 0.2 mm into a nozzle with an inner diameter of 80 μm. The electric field intensity at the apex of the tip assist mode can reach $7.1 \times 10^6$ V/m. Moreover, the tip-assisted E-jet printing printed an array of droplets with a size of 2.3 μm, and compared with no tip-assisted, the printing resolution was increased by nearly five times.

However, in the previous printing system, the ground electrode is located below the substrate. If the distance between the nozzle and the substrate is reduced, the electric field will be distorted, causing the printing

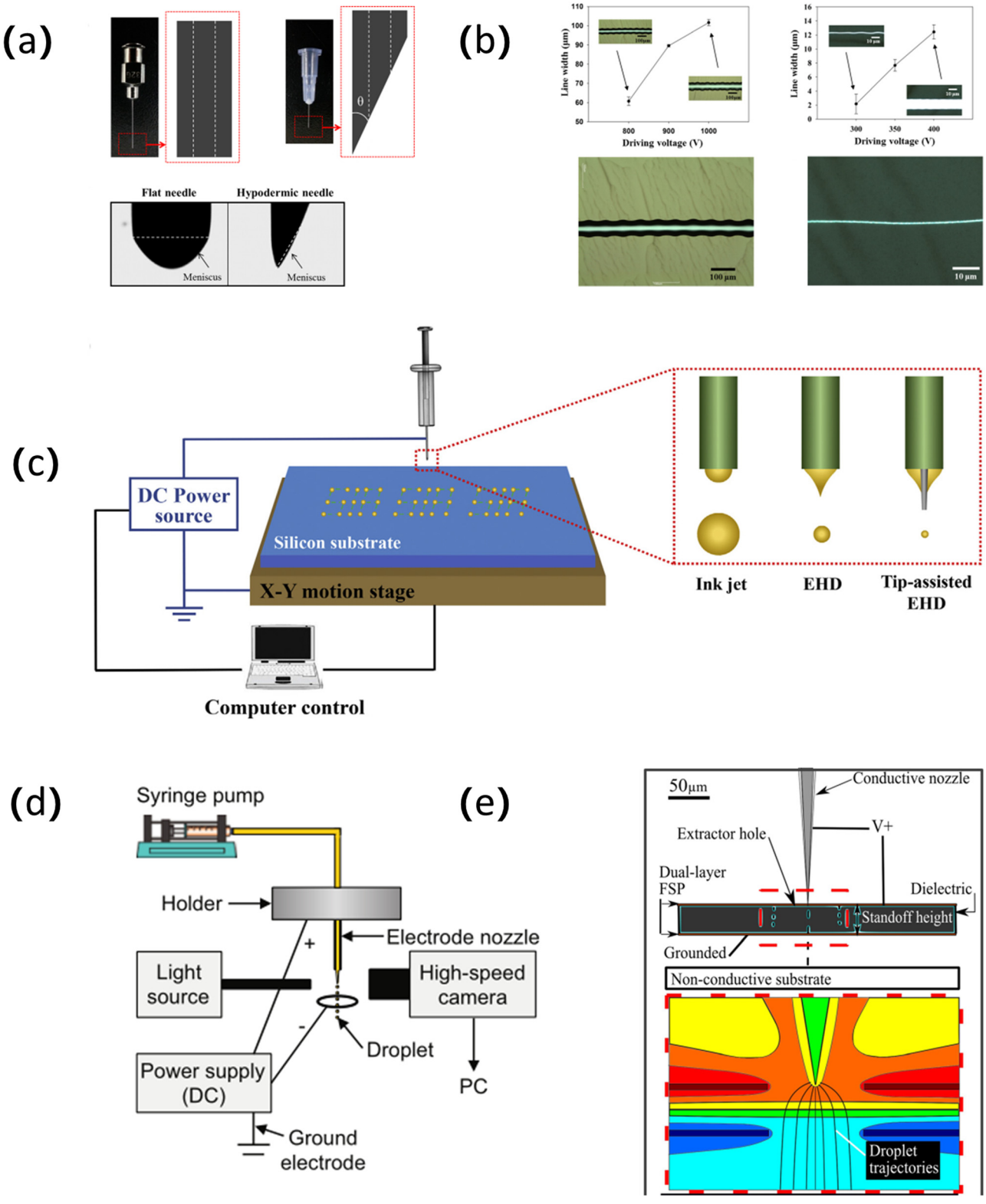


**Figure 7:** (a) Schematic diagram of the flat exit needle and hypodermic needle. (b) From left to right, the line width and shape changes of flat needles and hypodermic needles with increasing voltage. Reproduced from ref. [98] with permission from American Institute of Physics. (c) Tip-assisted E-jet printing system. Inkjet printing, E-jet printing, and tip-assisted E-jet printing nozzle tip jet comparison chart. Reproduced from ref. [100] with permission from Elsevier BV. (d) Schematic diagram of a printing device with metal ring electrodes. Reproduced from ref. [104] with permission from Elsevier. (e) Double conductive layer electric field forming print head and electric field line distribution. Reproduced from ref. [105] with permission from American Institute of Physics.

process to be unstable. Therefore, the distance between the nozzle and the substrate must be kept within a certain limit, which greatly limits the uniform printing on uneven and nonconductive surfaces. This limitation can be solved by designing a new type of print head in which the ground electrode is integrated into the print head [101–103]. As shown in Figure 7(d) [104], the printing system integrated with the nozzle and the metal ring extraction electrode is used to study the droplet generation characteristics of organic solvents with and without triglyceride oil [104]. An innovative nozzle design that integrates the nozzle and the ground electrode is proposed to solve the problem of printing on uneven surfaces [105]. As shown in Figure 7(e) [105], the field shaping design of the double-layer conductive layer separated by dielectric materials is adopted. The nozzle tip and the top conductive plate are connected to a positive voltage, and the bottom conductive plate is grounded. Finally, droplets with a resolution of less than 10 μm are obtained on uneven surfaces. Han and Dong [73] designed an integrated ring extractor as a ground electrode instead of a planar ground electrode to overcome the limitation of the height of the support in the 3D structure printing process. The diameter of the ring extractor is 4 mm and the distance from the nozzle is set to 300 μm. The 3D structure of polycaprolactol with a height of about 500 μm was successfully prepared by using the designed nozzle ring.

The low production rate of single-nozzle hinders the application of E-jet printing. Therefore, to improve production efficiency, nozzle design has attracted widespread attention, and various nozzle design studies have emerged, such as multinozzles [37,106,107], multihole nozzles [97], and coaxial nozzles [108–110]. Although multiple nozzles can effectively solve the problem of low throughput, the repulsion between adjacent nozzles will cause the meniscus at the nozzle to deflect outward, which is called end effect, as shown in Figure 8(a) [111]. The asymmetric electric field is the main cause of the end effect. At the same time, the reduction in the spacing between the nozzles leads to crosstalk between adjacent jets, which is a factor that aggravates the end effect [112]. Another important factor is the use of metal nozzles, which enhance the repulsive force between adjacent nozzles. Therefore, under the perplexity of these factors, research on the crosstalk problem of multinozzle E-jet printing has appeared. A multinozzle made of dielectric materials is used in the E-jet printing process. The distance between adjacent nozzles of 3 mm has been determined through testing, which minimizes the crosstalk between adjacent jets [113]. Choi *et al.* [114] used three independent ink supply channels and voltage sources and used a triangular nozzle array instead of a traditional linear nozzle array to reduce crosstalk, as shown in Figure 8(b) [114]. When the nozzle pitch is 3 and 5 mm, compared with the linear array, the offset of the meniscus of the triangular array from the nozzle center, that is, the spray angle, is reduced by about 30 and 60%. Parallel injection of nozzles can greatly improve the efficiency of patterning. For realization of separate control between different nozzles, Lee *et al.* [106] controlled three injection pumps to realize the independent control of a single nozzle. Using the clever mechanical design, Sutanto *et al.* [115] designed a rotating print head to switch between active and inactive nozzles. Each nozzle is fed with different ink materials, and the size of the droplets can reach the micron level, which can not only print with multiple nozzles but also allows multimaterial printing. In multinozzle E-jet printing, it is critical to improve the controllability of printing and to achieve the consistency of individual jets, jet sizes, and positions of each nozzle. For the purpose of improving controllability, a multilevel voltage, multiparallel nozzle addressable E-jet printing system is designed [116]. The print head is composed of a nozzle layer and an extractor layer. The conductive ring of the extraction layer can control each nozzle individually, as shown in Figure 8(c) [116]. By controlling the electric potential of the noninjecting conductive ring, researchers could reduce the interference of the electric field and enhance the electric field distribution of the injection nozzle. Then, a combination of one, two, and three injection nozzles is realized on the hydrophobic silicon wafer, and a droplet array with good size and position consistency is obtained, as shown in Figure 8(d) [116].

## 3.3 Ink characteristics

The ink is a hybrid material composed of functional materials and polymers, which plays a vital role in the jetting process. The study of ink characteristics (surface tension [61], density [117], viscosity, and conductivity [49,50]) helps to better understand the jetting process. Among them, the printing jet volume increases with the increase of viscosity and decreases with the increase of conductivity. A large conductivity corresponds to a small shear stress acceleration, and a smaller ejection volume is achieved. Therefore, the conductivity increases, the droplet diameter and the distance between adjacent droplets are reduced [118]. Kwon *et al.* [119] showed that drop-on-demand inkjet printing is a function of viscosity, conductivity, and surface tension, and to better characterize the performance of E-jet printing, especially the droplet

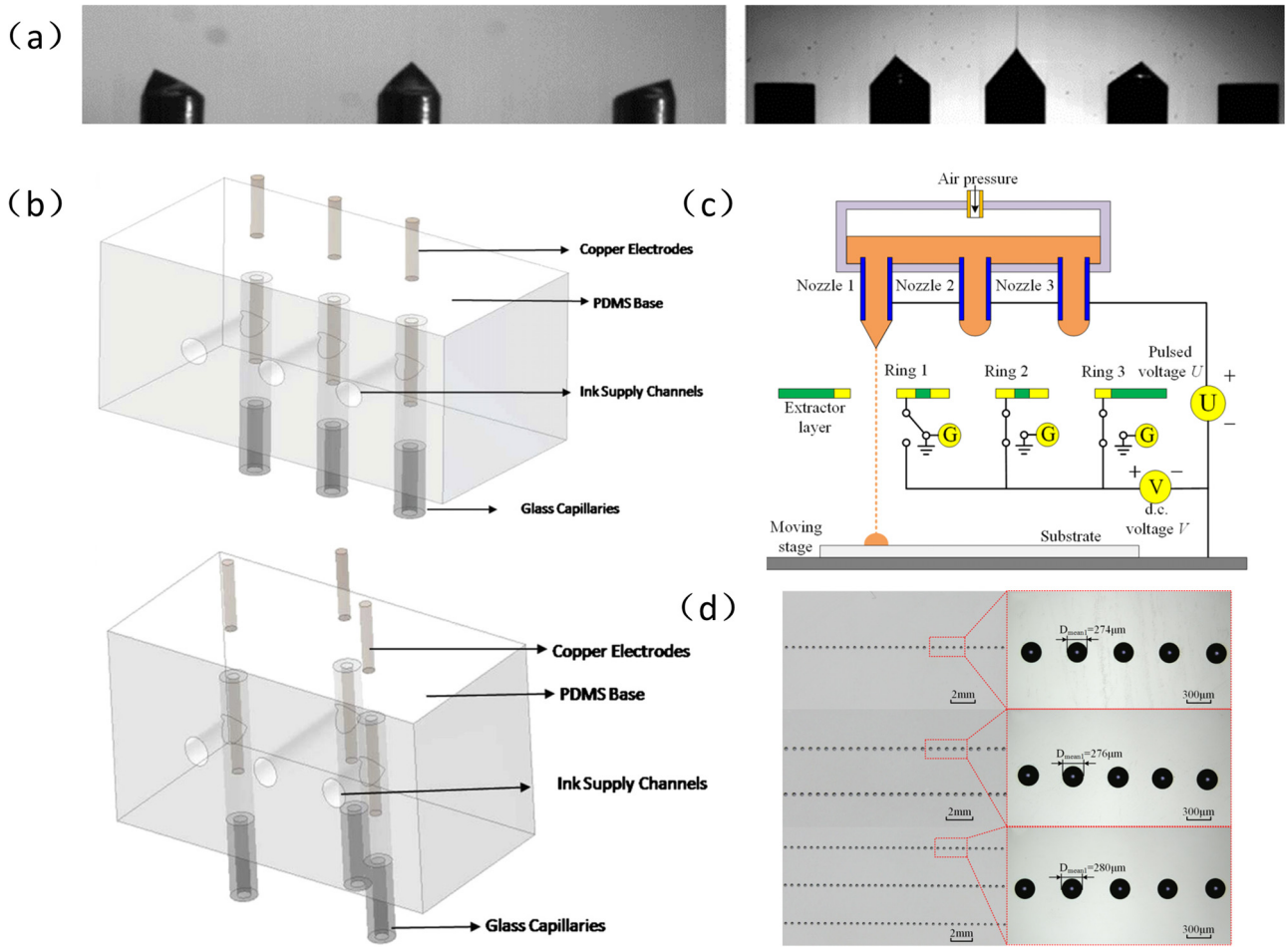


**Figure 8:** (a) End effect diagram. Reproduced from ref. [111] with permission from Elsevier. (b) Schematic diagram of linear and triangular array multinozzle print heads. Reproduced from ref. [114] with permission from Elsevier. (c) Schematic diagram of addressable E-jet printing with multilevel voltage parallel nozzles. (d) The array of droplets obtained by printing with one, two, and three nozzles. Reproduced from ref. [116] with permission from American Institute of Physics.

ejection frequency, a dimensionless universal coefficient containing the aforementioned three ink properties is defined. The pulse duration increases with increasing viscosity and decreases with increasing conductivity and surface tension. Larger particles in the ink will lead to the formation of satellite droplets, which will affect the resolution and the quality of the printing. Increasing the viscosity can effectively reduce the number of satellite droplets [50]. The size of the metal particles in the printing ink affects the ink configuration, which in turn affects the droplet behavior. Therefore, Huang *et al.* [120] used inks with three different particle configurations of small particle size, medium particle size, and large particle size to study the effects on droplet wetting diameter, height, contact angle, and impact velocity. The data show that under the action of an electric field, a large particle size brings a small droplet wetting diameter and a small contact angle, while a medium particle size has a higher initial impact velocity.

The core principle of E-jet printing is the formation of Taylor cone jets. Bae *et al.* [121] applied the same process parameters to seven solutions with different surface tensions. The results show that the ink surface tension affects the jet pattern of E-jet printing. At the same time, under the same electrostatic field, compared with polystyrene, polymethyl methacrylate with higher conductivity has faster charge convection, so the cone-shaped phase transition is faster and the conductivity is related to the change of the meniscus structure. As a key material property, ink viscoelasticity affects jet ejection. Yu *et al.* [122] designed two independent models of elasticity and viscosity. The dimensionless numbers $\xi$ and $\chi$ are used to represent the elasticity and the viscosity of the ink, and a dimensionless operating window diagram is drawn. Figure 9(a) [122]

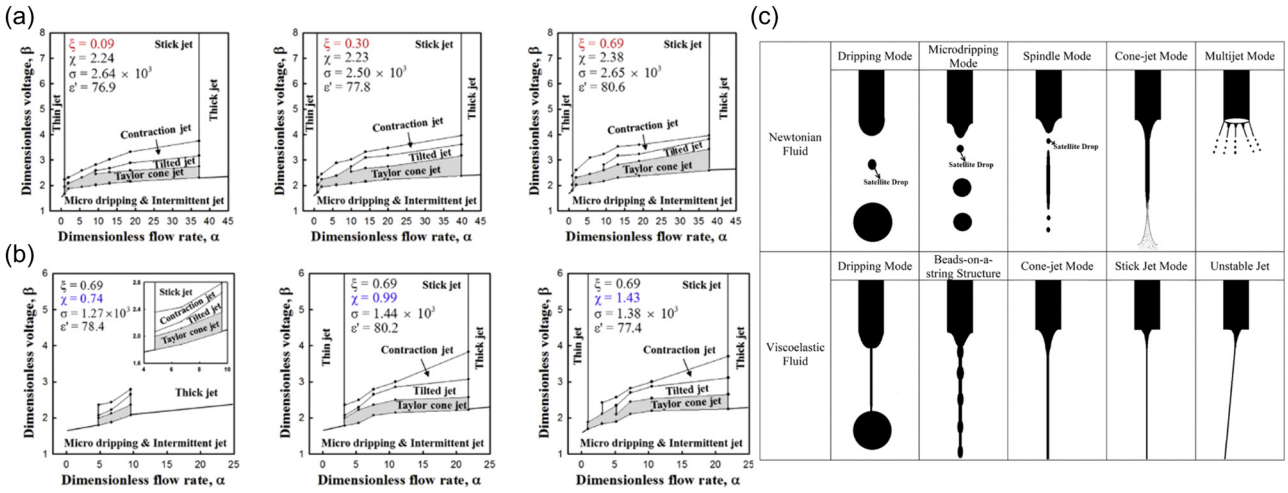


**Figure 9:** (a) From top to bottom, from left to right, the jet windows of six PEO solutions with different molecular weights: M03, M06, M10, M20, M40, and M50. For example, M10 represents a PEO solution with a molecular weight of $1.0 \times 10^6$ g/mol. (b) From top to bottom, from left to right, the jet window diagrams of six PEO solutions with different viscosities: C18, C24, C30, C38, C42, C52. For example, C18 means 0.18 wt% PEO solution. Reproduced from ref. [122] with permission from Elsevier BV. (c) Comparison of the jet modes of Newtonian fluid and viscoelastic fluid. Reproduced from ref. [123] with permission from American Institute of Physics.

shows that the increase in elasticity expands the voltage range of the Taylor cone jet. The study found that although elasticity delays the formation of the cone jet, it improves the stability of the jet cone shape. As shown in Figure 9(b) [122], when $\chi > 1$ and $\chi < 1$, the increase in viscosity broadens the voltage and the flow range of the Taylor cone jet, and the viscosity can be used to stabilize the Taylor cone jet. At the same time, the viscoelasticity of the ink leads to changes in the fluid dynamics behavior, resulting in a new E-jet printing mode that is different from Newtonian fluids, as shown in Figure 9(c) [123]. In the dripping mode, since the droplets exhibit strong elasticity, the droplets cannot immediately leave the nozzle and form filaments until they break. The second mode is the beaded mode, which can be observed only in viscoelastic fluids. The increase of the electric field results in the cone jet mode and the rod-shaped jet mode with a thinner jet. When the voltage reaches the unstable threshold, there is no branch at the lower end of the unstable jet because the viscoelasticity stabilizes the jet. As the concentration of the solution increases, the rod-shaped jet mode is stable in a wider range of the electrocapillary tube. Viscoelasticity and conductivity are one of the reasons for the instability of the cone jet. The Coulomb repulsion between the charges on the surface causes the instability of the jet, which depends on the electric field. Based on viscoelasticity and conductivity, polyisobutylene/polybutene (low conductivity and high viscoelasticity), silver nanoparticle ink (high conductivity and low viscoelasticity), and polyethylene oxide/water (high conductivity and high viscoelasticity) were chosen to study the starting position of the unstable whip motion [124]. The starting position of the whip motion decreases linearly with the electric field. In contrast, the polyethylene oxide/water solution is significantly affected by the electric field due to its high conductivity whip motion. Therefore, highly conductive inks are not suitable for stable E-jet printing.

# 4 Application of E-jet printing

## 4.1 Electronic devices

E-jet printing technology, as a mask-free additive manufacturing process, can print various functional materials onto flexible substrates, making printing technology unique in the rapid preparation of electronic devices effect. Although inkjet printing has become popular in printed electronic products, the rapid development of electronic products and the continuous improvement of resolution requirements make inkjet printing unable to meet the requirements. As a high-resolution printing technology, E-jet printing plays an important role in the preparation of electronic devices. The application of E-jet printing in the manufacture of flexible electronic devices (such as conductive electrodes, field-effect transistors, and sensors) is discussed (Table 2).

**Table 2:** Application of E-jet printing

| Application of E-jet printing | Advantages | Application examples |
|---|---|---|
| Electronic devices | | |
| Conductive electrodes | • Maskless | • Printed conductive silver traces with a size of 35 μm, calculated resistivity is $3.9 \times 10^{-8}$ Ω/m |
| | • Low-cost rapid production | • A silver grid/graphene hybrid transparent conductive electrode with a resistivity of about 25 μΩ/cm was fabricated |
| Transistor | • A wide range of functional materials | • ZnO thin film transistors (TFTs) |
| | • Suitable for unconventional substrates such as/stretchable substrates and uneven curved surfaces | • M-PEDOT:PSS electrode transistor |
| Sensors | • High resolution | • Resistive temperature sensor with resistivity of 23.35 μΩ cm was fabricated |
| | | • Humidity sensor with high sensitivity (85 kΩ/%RH) and responsiveness (0–80% RH) was fabricated |
| Bioprinting | | |
| Cells and extracellular matrix | • High resolution | • Pattern the fibrin protein |
| Tissue engineering scaffold | • Fabricating DNA and protein microarrays | • Living cells printing |
| | • High cell survival rate | • E-jet printing is widely used in the construction of 3D scaffolds for specific tissue types, such as cartilage, tendon, bone, and heart |

### 4.1.1 Printing patterned conductive electrodes

In the manufacture of electronic devices, the clear patterned electrode lines is an important part of the realization of high-performance circuits, and patterned conductive electrodes are crucial in achieving high integration of electronic devices. E-jet printing can directly print the conductive materials used for the electrodes, thereby realizing high-resolution electrode patterns. Wang *et al.* [125] achieved a printing distance of 50 μm through E-jet printing and printed conductive silver traces with a size of 35 μm. The measured and calculated resistivity is $3.9 \times 10^{-8}$ Ω/m. Figure 10(a) [125] shows the microstructure of the center and the edge of the printed stripes.

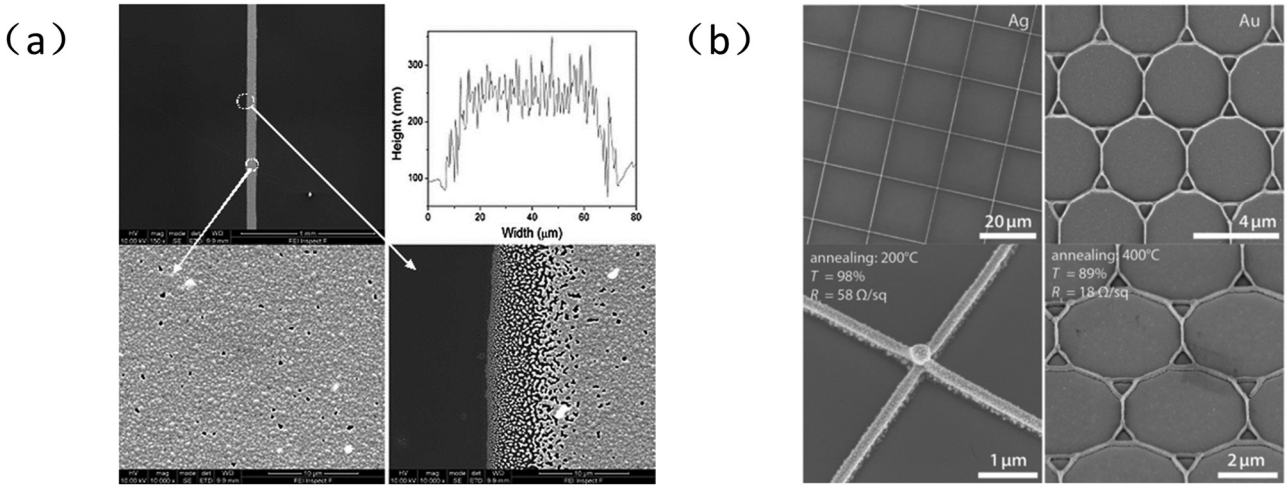


**Figure 10:** (a) Scanning electron microscopy image of printed silver traces on a silicon substrate after curing and cross-sectional profile measured by atomic force microscope. Reproduced from ref. [125] with permission from American Institute of Physics. (b) E-jet printed square silver grid electrode and gold grid electrode. Reproduced from ref. [132] with permission from Wiley-VCH Verlag.

There are more pores at the edge of the track, which is due to the repulsion of the charged droplets causing the satellite droplets to drop on the edge of the track. The silver nanoparticle ink is printed on the grapheme with good conductivity used as the substrate by E-jet, and a silver grid/graphene hybrid transparent conductive electrode with a resistivity of about 25 μΩ/cm can be fabricated [126]. Although the previous E-jet printing has successfully prepared patterned conductive lines, however, satellite droplet scattering effect in the printing process was still not solved. Wang *et al.* [127] used pulsed E-jet printing to produce a continuous conductive silver pattern with a diameter of 45–55 μm and a width of 60 μm. The droplet size increases as the voltage value increases, but high voltage will cause the ink to scatter during fabrication. The experiment determined an external pressure of 1.2 kV to avoid scattering. Son *et al.* [128] prepared metal wires with a width of 2.99 μm and a thickness of 0.23 μm by a combination of E-jet printing and laser sintering. At the same time, laser sintering is used to avoid thermal effects on the surrounding pattern lines, and a resistivity of 17.48 μΩ/cm is obtained.

Transparent electrodes are the key structure of various optoelectronic components. Due to its limited optical properties under low sheet resistance and brittleness, transparent conductive oxides, especially indium tin oxide, have gradually turned to alternative materials such as carbon nanotubes [129], graphene films, metal nanowires [130], and metal gate electrodes [90,131–133]. A silver grid transparent electrode with line width less than 10 μm is prepared [134]. The sheet resistance of the silver grid electrode is a function of the line spacing, which decreases with the decrease of the line spacing, but a small spacing means more silver grid lines, which leads to a decrease in transmittance. The study found that the silver grid spacing of 150 μm is the best spacing to achieve good electrical and optical performance, and the transmittance is 81.75%. Park and Hwang [90] used AC jet printing to prepare a flexible transparent silver grid on a polyester substrate. A silver grid with a line width of 27 μm was sintered at 180°C, and the light transmittance increased to 84.2%. The metal grid electrode printed by E-jet printing still balances the two aspects of electrical conductivity and light transmittance. Schneider *et al.* [132] used E-jet printing to print a metal gate with a high aspect ratio as a transparent electrode and obtained nanowalls with a line width of 80–500 nm and a height of 200 nm to 1.5 μm through layer-by-layer printing. As shown in Figure 10(b) [132], two different types of metal grid electrodes are fabricated. For the square grid electrode, the minimum sheet resistance is 8 Ω/sq at a transmittance of 94%. The high aspect ratio metal nano-gate achieves high transmittance while ensuring low sheet resistance.

The commonly used conductive material for E-jet printing electrodes is silver nanoparticles [66,113,135]. However, the high cost of silver materials limits the development, so finding cheap alternative materials is the direction of current efforts. Jeong *et al.* [136] prepared ZnO thin film transistors (TFTs) by thermal annealing electrospray acrylic (ZnA) film. Due to the low field-effect mobility of the original ZnO TFTs, the electrical properties are improved with the increase by adding a small amount of indium to ZnO, and it is determined that proportion of 1:0.1 is the best Zn/In precursor solution ratio. As shown in Figure 11(a) [136], the TFTs prepared by the MWCNT/PSS electrodes show similar output characteristics as the TFTs prepared by the aluminum electrodes. The TFTs prepared by Ag nanoparticles and PEDOT:PSS showed poor electrical performance and hysteresis. Copper precursors, poly(vinylpyrollidone) (PVP), and Cu(II)trifluoroacetate ($Cu(CO_2CF_3)_2CTA$) composite nanofibers are selected to be converted into copper nanofibers through a two-step calcination process [137]. As shown in Figure 11(b) [137], the parallel copper nanoelectrode with a diameter of 710 nm has a high transmittance of 98%. Li *et al.* [138] used copper particles based on end-capping agents to improve the stability of the suspended ink to achieve stable cone-shaped ejection. At the same time, polyethylene oxide (PEO) and copper of different molecular weights are mixed to adjust the viscosity of the ink, thereby limiting the diffusion effect of the droplets to obtain clearer lines. The printed lines get a direct electrode pattern after sintering in a strong second, and the copper/PEO electrode line is used as the field-effect transistor electrode, as shown in Figure 11(c) [138]. Although metal-based electrode materials have good conductivity, poor mechanical stability and unevenness of organic semiconductor films are the problems of organic thin film transistor electrodes. As a good organic electrode material, PEDOT:PSS is modified by dimethyl sulfoxide and surfactant to improve conductivity and surface tension [139]. The mixed PEDOT:PSS printed electrode lines of 150, 112, and 81 μm on bare substrate, HMDS substrate, and PS-b treated silica substrate as source and drain.

#### 4.1.2 Transistor

A transistor is an important part of flexible devices such as high-resolution display devices. Good electrical performance is an important factor to ensure the normal work of the device. The transistors made by E-jet printing

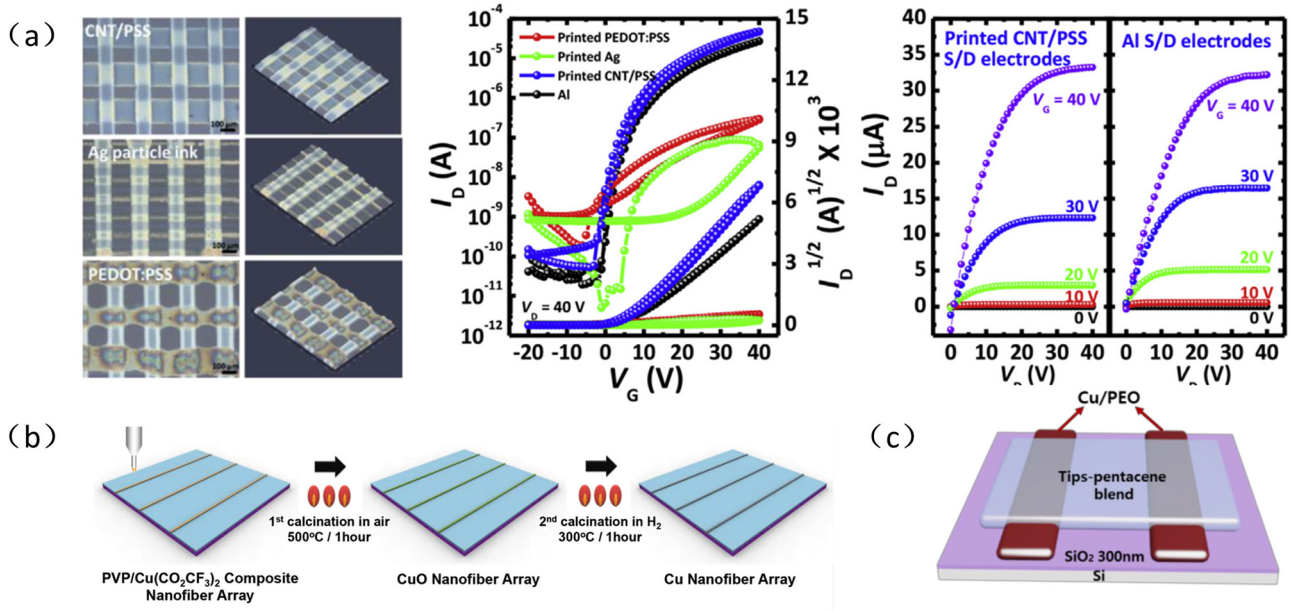


**Figure 11:** (a) ZnO: In thin film transistors made by E-jet printing with three kinds of conductive materials (MWCNT/PSS, Ag nanoparticles, and PEDOT:PSS) and transfer characteristics and output characteristics. Reproduced from ref. [136] with permission from Elsevier. (b) Diagram of the preparation process of the copper nanofiber array. Reproduced from ref. [137] with permission from Wiley-Blackwell. (c) Cu/PEO source/drain electrode field-effect transistors prepared by E-jet printing. Reproduced from ref. [138] with permission from Korean Society of Industrial Engineering Chemistry.

ensure the stability of electrical performance. The mobility, threshold voltage, and on/off current ratio of thin film transistors are three key parameters for evaluating the electrical performance. Lee and Choi [140] used E-jet printing to fabricate two ionic gel electrolytes of P3HT and PEDOT:PSS with pattern line widths of 10 and 200 μm. Ion gel transistors have average mobility, threshold voltage, and on/off current ratio of 0.12 ± 0.05 cm$^2$/V s, −0.83 ± 0.1 V, and $10^5$, respectively. Park *et al.* [139] prepared organic thin film transistors with two bottom contact structures of m-PEDOT:PSS electrode and Au electrode by E-jet printing as shown in Figure 12(a) [139]. The transfer characteristics and output characteristics of the transistor show that the field mobility of the transistor with m-PEDOT:PSS electrode is 0.157 cm$^2$/V s about three orders of magnitude higher than that of the Au electrode, and the output exhibits linear current-voltage characteristics. The study also found that the structural inhomogeneity in the Au electrode/channel interface limits the charge transfer, and the m-PEDOT:PSS electrode transistor has better electrical

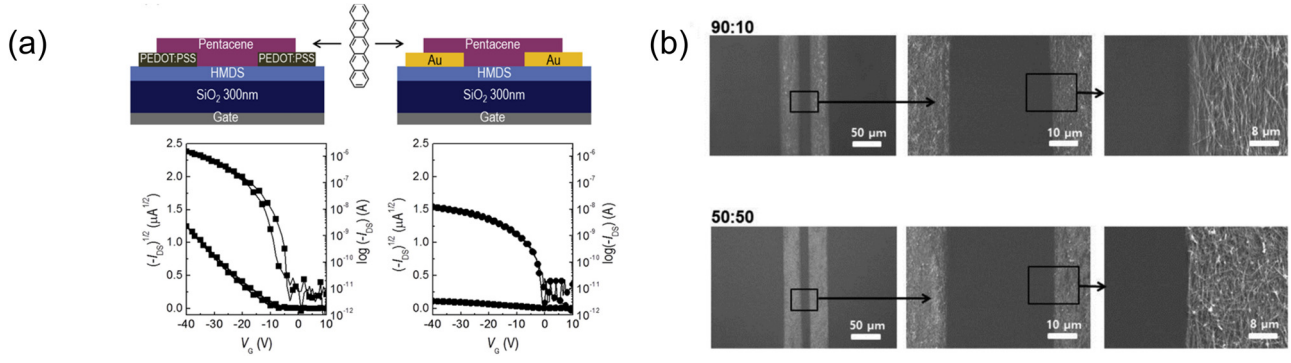


**Figure 12:** (a) Schematic diagram of the structure of organic thin film transistors with m-PEDOT:PSS and Au electrodes and their transfer characteristics and output characteristics. Reproduced from ref. [139] with permission from Elsevier. (b) S/D patterns made of AgNWs/PEO mixed materials with weight ratios of 90:10 and 50:50, respectively. The enlarged form of the interface between the electrode and the channel is shown in the rightmost image. Reproduced from ref. [141] with permission from Elsevier.

performance. Wang *et al.* printed PEDOT:PSS/carbon nanotube composite ink to achieve a minimum conductive channel length of 7 μm, and the field-effect mobility of the transistor is 0.03 ± 0.01 $cm^2$/V s. To achieve the cone-shaped ejection of silver nanoparticles (AgNWs), poly (ethylene oxide) (PEO) is added to increase the viscosity of the ink, which helps to fabricate silver nanopatterns with finer line widths. Experiments have proved that the 90:10 AgNWs/PEO composite is the better ink ratio that achieves high electrical conductivity [141]. The printed silver nanowires are used as the source/drain (S/D) electrodes of the transistor. The channel area between the two electrodes is free of pollution and maintains a stable pattern fidelity, as shown in Figure 12(b) [141]. The TIPS-pentacene/PS blend is used as the semiconductor layer of the transistor, and the AgNWs/PEO composite electrode is placed on the substrate to form a transistor. The average field-effect mobility, threshold voltage, and on/off current ratio of the photomultiplier tube are 0.51 $cm^2$/V s, −2.0 V, and $-10^6$, respectively.

Due to its high mobility, uniformity, and transparency, oxide thin film transistors have received widespread attention, and metal oxide semiconductors are considered a promising channel material [142–145]. Lee *et al.* [146] used an E-jet to print amorphous oxide indium zinc oxide (IZO), and Figure 13(a) [146] shows a schematic diagram of a transistor. The mobility of the device is 3.7 $cm^2$/V s, and the on/off current ratio exceeds $10^5$. The electrical performance of semiconductor devices depends on the precursor concentration and the composition ratio of indium to zinc. An increase in the molar ratio of indium to zinc causes a decrease in the on/off current ratio. The addition of formamide (FA) to the In–Ga–Zn–O (IGZO) precursor solution increased the field-effect mobility of the transistor by 4.3 times (from 2.4 to 10.4 $cm^2$/V s). Kim *et al.* [143] chose a representative oxide semiconductor indium oxide ($In_2O_3$) with high mobility and effective charge transfer for E-jet printing. Figure 13(b) [143] shows the E-jet printing auxiliary source/drain (S/D) printed $In_2O_3$ thin film transistors. Compared with the spin coating process and the inkjet printing method, E-jet printing shows very good electrical performance. At an annealing temperature of 500°C, the atomic rearrangement between semiconductors makes the mobility of ZTO thin film transistors up to 9.82 $cm^2$/V s, which is almost three times that of spin-on thin film transistors [140]. Compared with the 18 and 14 V

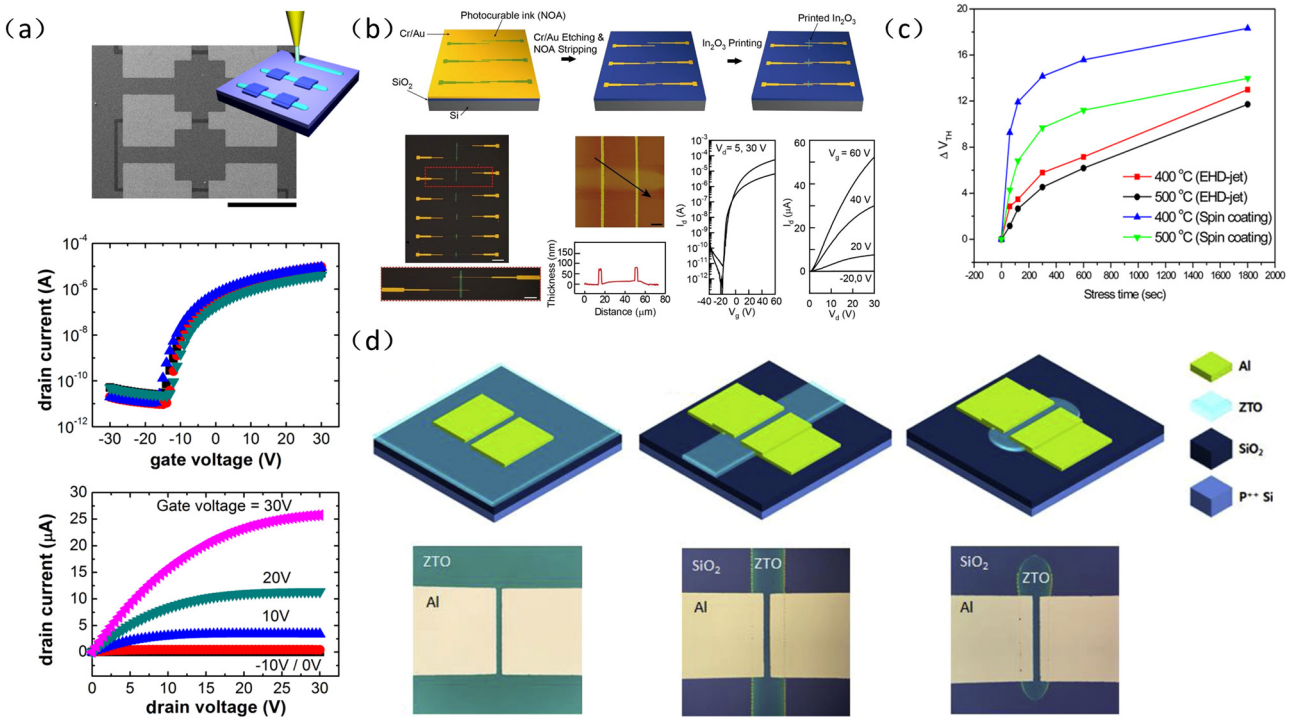


**Figure 13:** (a) The electrical characteristics of E-jet printed IZO TFTs. Reproduced from ref. [146] with permission from American Institute of Physics. (b) The electrical characteristics of E-jet printed IZO TFTs. Reproduced from ref. [143] with permission from Royal Society of Chemistry. (c) Comparison chart of threshold voltage offset over time for E-jet printing and spin coating processes. Reproduced from ref. [140] with permission from American Chemical Society. (d) Schematic diagram of TFT structure prepared by spin coating, maskless E-jet printing, and masked E-jet printing. Reproduced from ref. [144] with permission from Elsevier Ltd.

positive bias offset of spin coating at 400 and 500°C, the stability of the positive bias voltage of E-jet injection is significantly improved as shown in Figure 13(c) [140]. Figure 13(d) [144] shows that zinc-tin-oxide (ZTO) thin film transistors (TFTs) are prepared by spin coating, maskless E-jet printing (line printing), and masked E-jet printing (direct patterning). The ZTO film is completely covered by spin coating, the overlap area of the line printing ZTO is reduced, and the direct mask patterning of the ZTO causes the length to be reduced [144]. The drain cut-off current of the three methods is almost the same, but the gate leakage current is significantly different. The patterned ZTO of the semiconductor layer reduces the fringe field area, thereby reducing the gate leakage current, and the patterned thin film transistor can work stably under positive bias stress. The directly patterned ZTO TFTs showed a mobility of 7.0 $cm^2/V$ s and a threshold voltage of 7 V.

#### 4.1.3 Sensors

Direct printing of flexible and stretchable conductor materials provides a low-cost, mask-less manufacturing process for manufacturing flexible electronic devices. The preparation of the sensor array enables E-jet printing to prepare high-resolution flexible devices. Recently, many different types of sensors [147–150] such as temperature sensors, capacitive touch sensors, and gas sensors have been prepared using E-jet printing. Choi *et al.* [151] prepared a resistive temperature sensor by spraying silver nanoparticles onto a polyester substrate [151]. The temperature rise causes the resistance of the wire to increase. The resistivity of the printed temperature sensor is 23.35 μΩ cm. To improve the sensitivity and the sensing range of the humidity sensor, the graphene/methyl red composite material is deposited on the interdigital electrode as the sensing layer [152]. The schematic diagram of the humidity sensor is shown in Figure 14(a) [152]. The resistance of the sensing layer decreases as water vapor acts on the surface, and the change in resistance is collected by the digital electrode. For a relative humidity of 5–95%, the resistance value is reduced from 11 to 0.4 MΩ, and the resistance sensitivity could reach 96.36%. This humidity sensor shows good sensitivity, response time (0.251 s), and recovery time (0.35 s). Zeeshan Yousaf *et al.* [153] printed a 10 μm zigzag microelectrode as a temperature sensor and a 5 μm interdigital sensor electrode for a humidity sensor. After the electrode is prepared, the humidity sensor is made by electrostatic spraying the active layer of the composite material of polyethylene oxide and molybdenum disulfide. The corresponding humidity sensor of this composite material is almost linear, showing high sensitivity (85 kΩ/% RH) and responsiveness (0–80% RH). The humidity sensor is inevitably affected by the environmental temperature, and a mathematical model of temperature and relative humidity is established. According to the mathematical relationship, the relative humidity compensation of the temperature effect can be realized [153]. Capacitive touch sensors recognize contact behavior by detecting small changes in charge caused by contact. Qin *et al.* [154] prepared a capacitive touch sensor with an interdigital electrode structure and at the same time studied the influence of design parameters on electrical performance. The capacitance increases with the number of electrodes, the length of the electrodes, and the distance between the electrodes. Subsequently, the sensitivity of the sensor was tested in terms of finger contact and droplet deposition [155]. Han and Dong [156] used E-jet to print molten metal alloy ink to manufacture a high-resolution, high-density capacitive touch sensor array with a resolution of less than 50 μm. The capacitor is composed of a high-resolution metal grid of uniform line width, and the small size of the metal wire helps to minimize the small change in the capacitance of each sensor.

Due to the increasing air pollution and the existence of various dangerous gases in industrial production, the importance of gas monitoring is obvious. Most gas sensors obtain sensing data by measuring changes in the resistance of the sensing material. To achieve a highly integrated and compact environmental gas sensor, four metal oxide ($SnO_2$, $In_2O_3$, $WO_3$, and NiO) nanofibers are used for E-jet printing to prepare resistive gas sensors [157]. The integrated gas sensor array can detect $NO_2$ and $H_2S$ gases with a power consumption of 20 mW. The reduced area of the sensing material helps to reduce the power required for heating and sensing. The integrated gas sensor array made of three oxide materials of $SnO_2$, $WO_3$, and $In_2O_3$ is shown in Figure 14(b) [157]. Under the same conditions for $NO_2$ detection, the sensitivity of $SnO_2$, $WO_3$, and $In_2O_3$ to $NO_2$ are 35, 19, and 15, respectively. Therefore, the use of sensor data graphic analysis and principal component analysis can roughly identify unknown gases. The mini hot plate (MHP) gas sensor has attracted widespread attention due to its small size and low power consumption. Wu *et al.* [158] used E-jet to print the MHP hydrogen sensor, and the MHP sensor obtained the highest response and low power at 185°C. Zhang *et al.* [159] used layer-by-layer self-assembled graphene oxide (GQ), and the electric field-induced arrangement helped the formation of the layered structure and obtained a flat morphology. Figure 14(c) [159] shows the preparation process of a high aspect ratio

3D ammonia sensor. First, E-jet prints a metal grid of silver nanoparticles and then sprays GQ to cover the 3D substrate to obtain an ammonia sensor through oxidation and reduction. The response and sensitivity of the sensor can be reflected by the change of resistance. For a sensor with a large aspect ratio, the resistance change can reach more than 70% due to the large reaction area, which shows the good performance of the E-jet printing high aspect ratio sensor.

## 4.2 Bioprinting

Bioprinting allows the patterning of different biomolecules, usually high-resolution patterning of various types of biomaterials or cells. Due to the sensitivity of biological materials, the choice of the preparation process is limited. For example, the printing of light-based microstructures/nanostructures is limited to specific photopolymers, and this process usually requires the support of expensive optical systems. However, E-jet-based bioprinting has good compatibility with various biopolymers and can achieve high resolution. Optimizing the corresponding process parameters to achieve a single flow of materials is helpful for the controllable deposition of biological materials at designated locations and precise regulation of cell behavior. Furthermore, the printing nozzle moves according to a specific program to realize the 3D structure manufacturing of layer-by-layer stacking. The controlled manufacturing of 3D microstructures/nanostructures allows the printing of biomimetic structure tissue scaffolds.

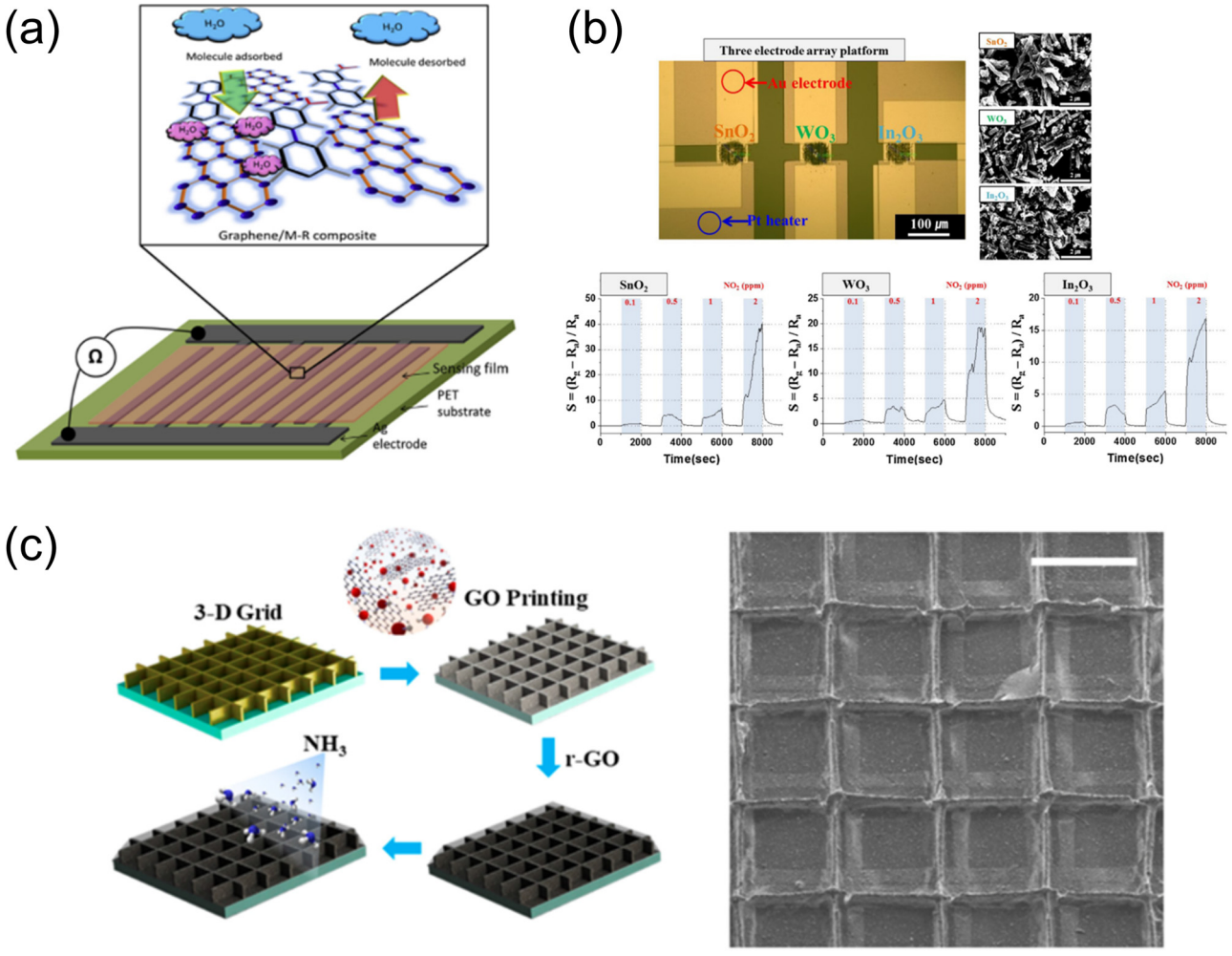


**Figure 14:** (a) A schematic diagram of a humidity sensor and an illustration of the phenomenon of water vapor interacting with the surface of the sensor. Reproduced from ref. [152] with permission from Elsevier Ltd. (b) Three gas sensor arrays made of $SnO_2$, $WO_3$, and $In_2O_3$ materials. The sensing results of three kinds of sensors for $NO_2$. Reproduced from ref. [157] with permission from Elsevier. (c) The structure diagram 3D ammonia sensor. Reproduced from ref. [159] with permission from MDPI (Basel, Switzerland).

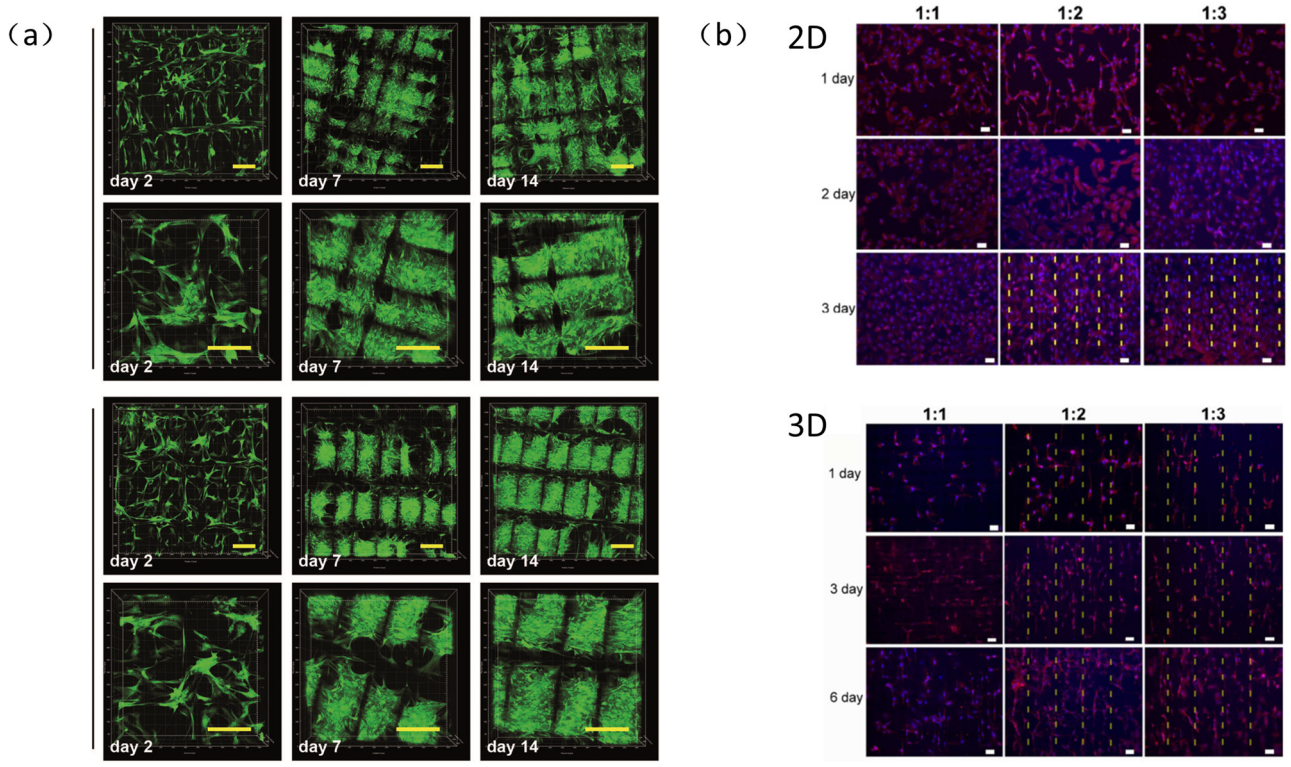


**Figure 15:** (a) From top to bottom, the growth of hESC-fibroblasts after cultured on the prepared PCL scaffold and PCL/chitosan scaffold for 2, 7, and 14 days, respectively. Reproduced from ref. [166] with permission from SAGE Publications Ltd. (b) Cell morphology images after 1, 3, and 6 days of culture on 2D and 3D scaffolds. Reproduced from ref. [28] with permission from Royal Society of Chemistry.

### 4.2.1 Cells and extracellular matrix

In the biological field, the cell is guided by various signals in the microenvironment, and the preparation of a controllable cell culture substrate is helpful for further understanding of cell biology. The hydrogel has excellent porosity and biocompatibility so that it can mimic the natural extracellular matrix, and the composition, structure, and mechanical properties of the hydrogel are easy to adjust. For example, fibrin, collagen, hyaluronic acid, and matrix gel are often used as cell carriers and scaffolds [160–163]. Poellmann *et al.* [164] utilized E-jet printing to pattern the fibrin protein on the polyacrylamide substrate, and the cells only adhere to the area modified by the extracellular matrix protein. However, the natural extracellular matrix has low mechanical stability, and it is difficult to adjust its structure and performance. Poellmann and Johnson [165] printed polyacrylamide, and after photopolymerization, the surface was filled with another hydrogel backfill. After the hydrogel substrate is patterned with collagen and fibronectin, MC3T3E1 preosteoblasts are coincubated. The porous structure of the scaffold providing nutrients and gas exchange required for cell growth allows cells to proliferate. Wu *et al.* [166] printed polycaprolactone stents with an average porosity of about 74% and dip-coated natural polymer chitosan onto the polycaprolactone stents to increase the hydrophilicity. The printed polycaprolactone and polycaprolactone/chitosan 3D scaffolds were used to culture human embryonic stem cell fibroblasts. As shown in Figure 15(a) [166], as time increases, the cells grow along the fibers or pass through the pores of the scaffold. At 14 days, cell aggregates almost occupied the entire scaffold, and the density of cells cultured on the scaffold coated with chitosan was slightly higher. The cell culture and proliferation efficiency is affected by the surface morphology and structure of the scaffold. Liu *et al.* [28] printed polylactic acid–glycolic acid copolymer (PLGA) to prepare 2D and 3D scaffolds with aspect ratios of 1:1, 1:2, and 1:3 and used the fabricated scaffolds to culture fibroblasts to study the influence of structure on cell behavior. For both 2D and 3D scaffolds, the proliferation effect of fibroblasts is better on the 1:2 and 1:3 structures. Better longitudinal extension and aggregation of the fibers are observed on the 1:2 scaffold. Compared with the 2D structure, the 3D scaffold shows a better arrangement. As shown in Figure 15(b) [28],

it shows a slight arrangement after 1 day of culture, and the cell angles of the 1:2 and 1:3 scaffolds are more uniform, indicating a high-level directional arrangement. Polycaprolactol stents with linear, serpentine, and hybrid structures are manufactured by changing the applied voltage, the distance from the nozzle to the substrate, and the flow rate [167]. The hybrid stent was made into the bottom coiled fiber under a voltage of 3.1 kV, and then the voltage was reduced to 2.5 kV to print the straight fiber. Although the linear scaffold has a porosity as high as 88%, the large pores limit the cell proliferation rate, and the serpentine-shaped small pore size makes nutrient penetration and gas exchange difficult. Serpentine and hybrid scaffolds increase the number of cells significantly more than linear scaffolds during cell culture for 3 to 7 days. In general, the better porosity and specific surface area of hybrid scaffolds are more beneficial to cell adhesion and proliferation.

In addition, the printing of living cells is an innovative research direction. The main problem based on E-jet printing is the viability of cells under the coupling action of electric field force, surface tension, and other forces. Previous studies [168–170] have shown that E-jet can be used to print living cells. The jetted cells can remain intact and viable and can proliferate normally, proving that high current and pressure do not damage the basic activities and structures of cells. The mixture of hydrogel and living cells as jet inks can be used for the controllable fabrication of high-resolution patterns and structures in bioprinting [171,172]. Gasperini *et al.* [173] used the E-jet process to print alginate hydrogels containing living cells. After being labeled with staining reagents, it can be observed that the cells are maintained and evenly distributed after 1 day and 7 days of culture, as shown in Figure 16(a) [173]. Wang *et al.* [174] used E-jet printing technology to encapsulate single cells in algae hydrochloric acid hydrogel microspheres. Research of printing parameters found that the flow rate and the nozzle diameter have a significant impact on the size of the

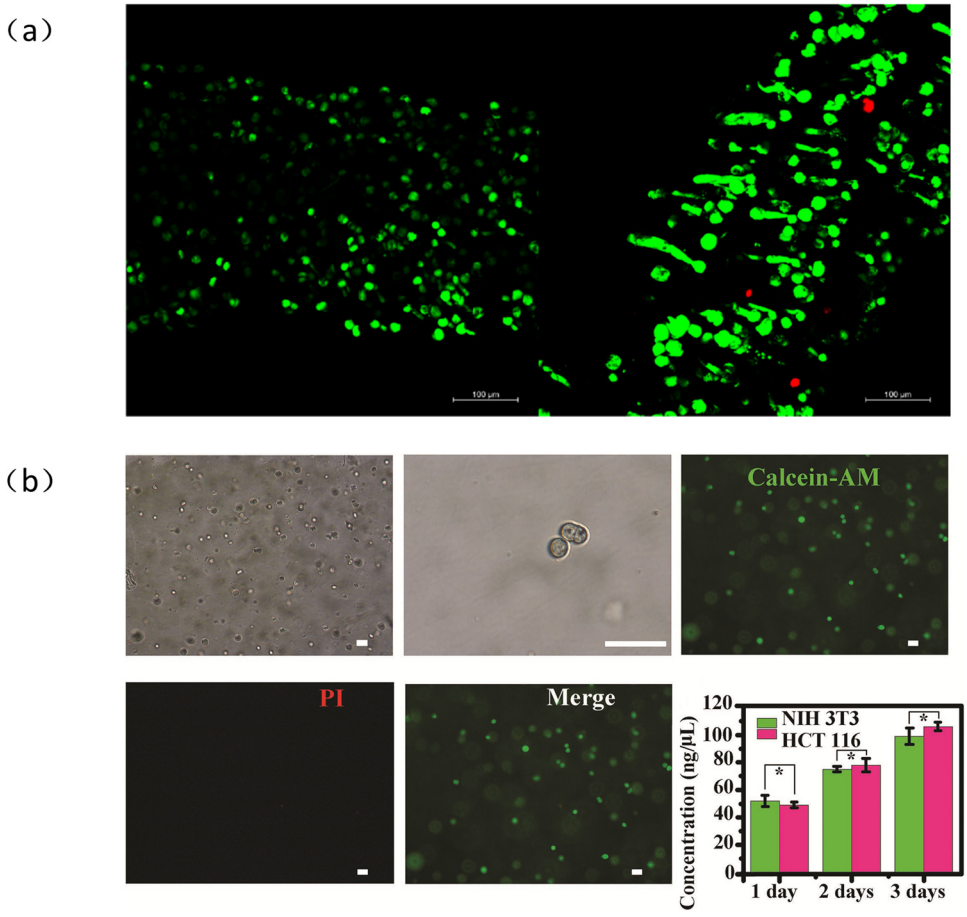


**Figure 16:** (a) Microscopic observation of cell viability after 1 and 7 days of cultured cells in alginate hydrogel containing living cells. Reproduced from ref. [173] with permission from Mary Ann Liebert Inc. (b) Cell growth and survival in bioink. Reproduced from ref. [174] with permission from Wiley-VCH Verlag.

microspheres. Microspheres within 100–600 μm diameter could be fabricated by changing parameters. Figure 16(b) [174] shows that the printed cells are evenly dispersed in the bioink after proliferation. After 7 days, the survival rate of the cells is about 98%, indicating the feasibility of culturing the cells encapsulated in hydrogel microspheres.

### 4.2.2 Tissue engineering scaffold

The fiber orientation scaffolds fabricated using E-jet printing is very similar to those of natural extracellular matrix, which provides guidance for cell contact and cell arrangement, so as to promote cell proliferation and tissue formation with the best porosity and pore size. Due to the mechanical properties of scaffolds and the advantages of guiding cell behavior, E-jet printing is widely used in the construction of 3D scaffolds for specific tissue types, such as cartilage [175,176], tendon [177,178], bone [179–184], and heart [185,186]. In the treatment of bone repair, poly($\varepsilon$-caprolactone) (PCL) has shown good application ability in bone growth and bone regeneration. An improved E-jet process using poly (ethylene oxide) (PEO) as the target solution bath produced a stable PCL scaffold with a pore size of about 347 μm and a porosity greater than 70% [179]. The successful culture of osteoblast-like cells (MG63) shows the potential ability of the PCL scaffold in bone tissue. Abbasi *et al.* [184] successfully printed a porous scaffold for tissue culture of human osteoblasts. Based on changes in bone density, a heterogeneous patterned scaffold containing gradient porosity simulates the cancellous bone, while denser areas simulate hard cortical bone. As shown in Figure 17(a) [184], this 3D polycaprolactone scaffold is a three-layer (250 μm bottom to 500 μm middle to 750 μm top) gradient aperture bracket with three uniform pores and two fiber offsets (30/70 and 50/50%). The 250 μm pore size scaffold had the highest osteoblast adhesion, and the gradient scaffold showed the best proliferation ability. E-jet printed fibers with a curled shape similar to collagen fibers in natural tendons [178]. Figure 17(b) [178] shows the prepared straight fiber scaffold and crimped fiber scaffold. After tenocyte culture, it is found that the crimped fiber achieves a wider distribution of the nucleus angle, so the crimped fiber scaffold has a great potential in tendon tissue. The cell orientation of different layers of natural cardiomyocytes changes gradually. To simulate the structure of this type of cardiomyocyte tissue in different orientations, Mao *et al.* [186] used printed microlattices with specific layer orientations. The spacing of the microstructures and the number of printed layers are the keys to the formation of dense and highly arranged cell bands. As shown in Figure 18(a) [186], the human umbilical vein endothelial cell-collagen suspension is added to the 3D microstructure in a specific orientation. In addition, H9C2 cardiomyocytes, C2C12 skeletal muscle cells, and NHDF normal skin fibroblasts cells can also be successfully cultured on the scaffold. Similarly, multiple types of cells can also be closely arranged on the same scaffold. Figure 18(b) [186] shows the specific structure of the three layers with different orientations at an angle of 60°, and the cells in the bottom layer show a better arrangement.

Poly($\varepsilon$-caprolactone) (PCL) is the most commonly used material for E-jet printing, which has good biocompatibility, biodegradability, and ideal mechanical properties. However, PCL is limited by its hydrophobicity in tissue engineering applications, which seriously affects the adhesion

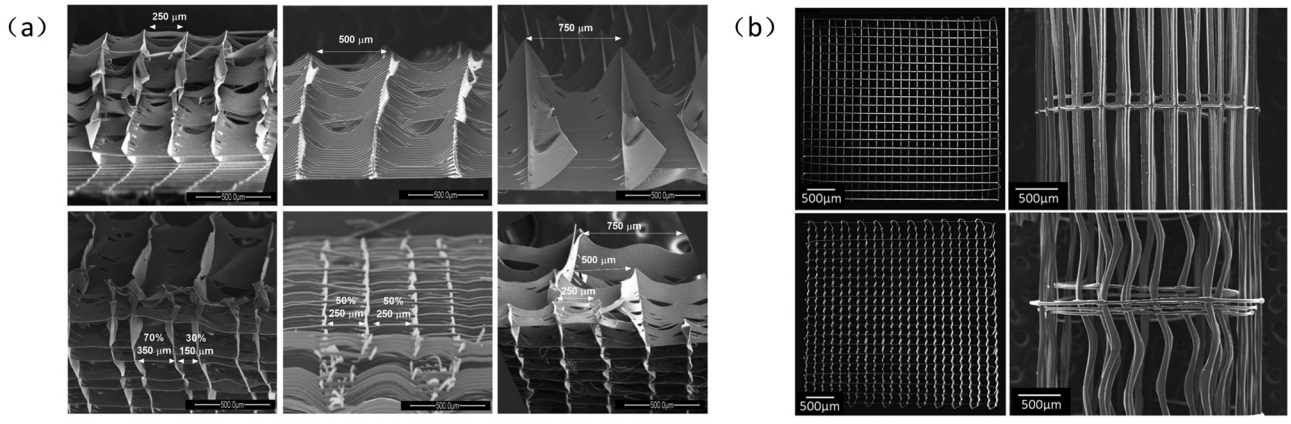


**Figure 17:** (a) The brackets with six square holes: from top to bottom, from left to right, the brackets with hole sizes of 250, 500, and 750 μm in sequence, the offset brackets with 30 and 50% offset between layers and three different gradient scaffold with a pore size (250/500/750 μm). Reproduced from ref. [184] with permission from American Chemical Society. (b) Images of straight fiber and curved fiber scaffolds. Reproduced from ref. [178] with permission from Elsevier BV.

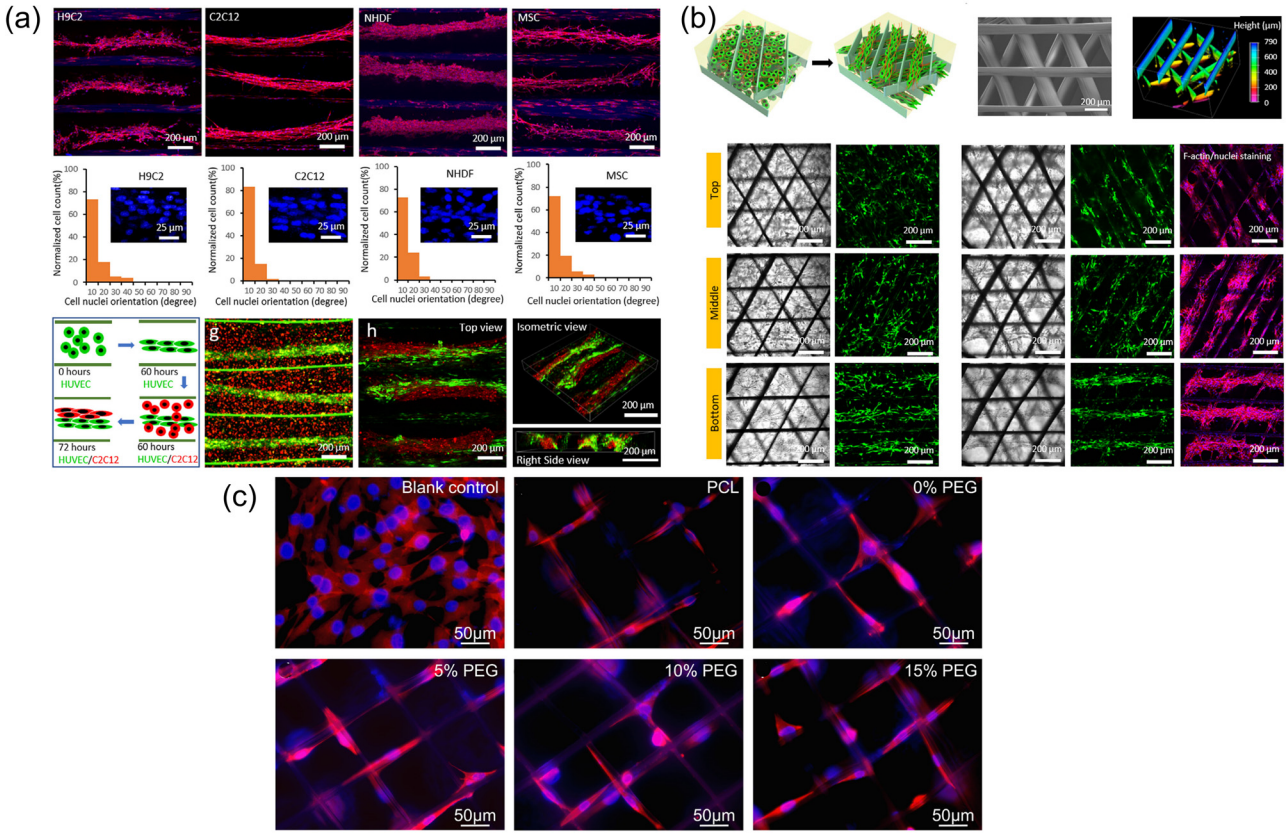


**Figure 18:** (a) The cell growth arrangement image of a single cell type or a plurality of mixed cells cultured in a curved array with 50 printing layers and a pitch of 600 μm. (b) Schematic diagram of the arrangement of three-layer scaffolds with different orientations and the activity and morphology images of HUVECs cultured in the bottom, middle, and top three layers. Reproduced from ref. [186] with permission from Elsevier BV. (c) The cell adhesion situation of the stent-free control group, pure PCL stent, and PEG content of 0, 5, 10, and 15% mixed ink stents. Reproduced from ref. [191] with permission from Elsevier.

and the growth of cells. Moderate hydrophilicity plays an important role in cell adhesion and proliferation [187]. Therefore, the research of adding hydrophilic biomaterials to make composite scaffolds fabricated using PCL materials has attracted attention [30,188–191]. He *et al.* [189] added PEO to PCL to adjust the solution viscosity to stabilize the E-jet printing process, and multiwalled carbon nanotubes (MWCNTs) were added to the composite solution to prepare PEO-PCL-MWCNT scaffolds. Compared with the PEO-PCL scaffold, although the PEO-PCL-MWCNT scaffold is not conducive to cell attachment, MWCNT helps the cells elongate along the fiber direction. Vijayavenkataraman *et al.* [30] printed polycaprolactone/polyacrylate (PAA) composite scaffolds and prepared the scaffolds with three different concentrations (2.5, 5, and 7.5%) of composite materials. The addition of PAA not only reduces the water contact angle but also accelerates the degradation rate. By changing the PCL/PAA concentration ratio, the mechanical properties and biodegradation rate can be adjusted to adjust the rate of tissue regeneration. Bai *et al.* [191] prepared PCL/polyethylene glycol (PEG)/roxithromycin (ROX) composite scaffolds by melt E-jet printing technology. The hydrophilicity of the composite stent was evaluated by measuring the water contact angle. As the content of PEG increased from 5 to 15%, the water contact angle decreased from 86.5° to 66.7°. The result indicates that PEG increased the hydrophilicity of the stent surface. At the same time, the addition of PEG speeds up the release rate and amount of ROX to a certain extent, thereby enhancing the antibacterial activity against *Escherichia coli* and *Staphylococcus aureus*. Human osteosarcoma cells (MG63) were cultured on the scaffold, as shown in Figure 18(c) [191]. Compared with the pure PCL scaffold, the cells on the surface of the composite scaffold and the fiber sidewall adhered more.

## 5 Summary and prospective

As a new type of additive manufacturing process, E-jet printing technology uses an electric field to induce fluid

movement, showing outstanding advantages and broad application prospects in terms of accuracy, resolution, materials, and cost. A theoretical analysis of the formation process of the jet and the deposition process of the droplets is necessary. There are many factors that affect E-jet printing resolution, mainly including process parameters [79,80,93,192] (voltage intensity, type of driving voltage, flow rate, distance from nozzle to substrate, moving speed of worktable), nozzle design [110,113,193], and ink properties [118,119,123] (conductivity, viscosity, density, and surface tension). In addition, environmental factors such as temperature and humidity also play a certain role in the process of droplet formation. These factors interact and couple with each other to promote cone jet formation and droplet deposition. To further improve the resolution and quality of the E-jet printing process and print high-resolution patterns, it is necessary to deeply understand the mechanism of E-jet printing, and the research on these factors is indispensable. This article summarizes the research progress of Taylor cone formation and stability. The instability of the jet process restricts the development of E-jet printing. At the same time, the coupling effects of various parameters on the system are also summarized separately, because the subtle changes of each parameter can easily cause a difference in the system. The optimization of these parameters and factors enables E-jet printing to be applied to many fields. Electronic devices fabrication [156,194–197] is one of the applications of E-jet printing. The main limitation of flexible devices is that the incompatibility of high-viscosity inks and semiconductor materials makes it difficult to achieve high-resolution pattern printing. The biological field [31,197–199] is another promising application of E-jet printing. E-jet printing can print biological materials with good biocompatibility, which realistically simulates the original tissue of the natural extracellular matrix. This article reviews the manufacturing applications of E-jet printing technology in electronic devices (conductive electrodes, transistors, and sensors) and biology (cells and extracellular matrix, tissue engineering scaffolds). In short, E-jet printing is a very effective process for realizing multimaterial, high-resolution, and high-quality noncontact manufacturing.

In the study of many coupling influencing factors of E-jet printing, environmental factors such as temperature and humidity also affect the ejection process, but research on the environment has not been well developed. First, it is necessary to study ejection formation and deposition under the combined influence of environmental effects and other factors. Second, to improve the efficiency of jet printing, multinozzle designs have gradually emerged, but as the number of nozzles increases, the disturbance between jets also increases. The number of nozzles is limited, and the efficiency of printing is still limited. Therefore, it is worth considering how to improve printing efficiency while ensuring high-resolution printing. At the same time, the decrease in the spacing between nozzles leads to increased disturbances. Although the increase of the distance can effectively reduce the disturbance, it will increase the difficulty of the design. Therefore, the multinozzle structure arrangement design should be considered in some detail. The deposition of 2D or 3D microstructures/nanostructures on flexible curved surfaces still needs further development. Materials like PCL can be mixed with other biomaterials, but this has a negative impact on the purity and mechanical properties of the printed structure. Therefore, it is important to develop innovative biomaterials to foster new applications. In other words, to further expand the scope and the depth of E-jet printing for the existing and new applications, research efforts will be needed to develop new printing systems combined influence of environmental effects and novel printing processes and to achieve in-depth understanding of the process–material interaction.

**Acknowledgements:** The authors wish to acknowledge the funding provided by the National Natural Science Foundation of China (Project No. 61803323), Shandong Province Natural Science Foundation (Project No. ZR2019BF049), and Joint fund of Science & Technology Department of Liaoning Province and State Key Laboratory of Robotics (Project No. 2021-KF-22-03).

**Funding information:** National Natural Science Foundation of China (Project No. 61803323), Shandong Province Natural Science Foundation (Project No. ZR2019BF049), and Joint fund of Science & Technology Department of Liaoning Province and State Key Laboratory of Robotics (Project No. 2021-KF-22-03).

**Author contributions:** W.Y., Y.S., and S.C. proposed the original idea and planned the configuration; Y.S. wrote the manuscript; Z.W., W.Y., S.C., and H.Y. revised the paper for language and quality. All authors have accepted responsibility for the entire content of this manuscript and approved its submission.

**Conflict of interest:** The authors state no conflict of interest.

**Data availability statement:** Data sharing is not applicable to this article as no datasets were generated or analyzed during the current study.

# References


[1] Barcelo S, Li Z. Nanoimprint lithography for nanodevice fabrication. Nano Converg. 2016;3(1):21.

[2] Lin Y, Gao C, Gritsenko D, Zhou R, Xu J. Soft lithography based on photolithography and two-photon polymerization. Microfluid Nanofluid. 2018;22(9):97.

[3] Yang L, Wei J, Ma Z, Song P, Ma J, Zhao Y, et al. The fabrication of micro/nano structures by laser machining. Nanomaterials. 2019;9(12):1789.

[4] Li Y, Hong M. Parallel laser micro/nano-processing for functional device fabrication. Laser Photon Rev. 2020;14(3):1900062.

[5] Zhang P, Wang Z, Li J, Li X, Cheng L. From materials to devices using fused deposition modeling: a state-of-art review. Nanotechnol Rev. 2020;9(1):1594–609.

[6] Dankoco MD, Tesfay GY, Benevent E, Bendahan M. Temperature sensor realized by inkjet printing process on flexible substrate. Mater Sci Eng: B. 2016;205:1–5.

[7] Mattana G, Loi A, Woytasik M, Barbaro M, Noël V, Piro B. Inkjet-printing: a new fabrication technology for organic transistors. Adv Mater Technol. 2017;2(10):1700063.

[8] Gao M, Li L, Song Y. Inkjet printing wearable electronic devices. J Mater Chem C. 2017;5(12):2971–93.

[9] Mikolajek M, Reinheimer T, Bohn N, Kohler C, Hoffmann MJ, Binder JR. Fabrication and characterization of fully inkjet printed capacitors based on ceramic/polymer composite dielectrics on flexible substrates. Sci Rep. 2019;9(1):13324.

[10] Ling H, Chen R, Huang Q, Shen F, Wang Y, Wang X. Transparent, flexible and recyclable nanopaper-based touch sensors fabricated via inkjet-printing. Green Chem. 2020;22(10):3208–15.

[11] Hu X, Yang Z, Kang S, Jiang M, Zhou Z, Gou J, et al. Cellulose hydrogel skeleton by extrusion 3D printing of solution. Nanotechnol Rev. 2020;9(1):345–53.

[12] Singh M, Haverinen HM, Dhagat P, Jabbour GE. Inkjet printing – Process and its applications. Adv Mater. 2010;22(6):673–85.

[13] Alamán J, Alicante R, Peña JI, Sánchez-Somolinos C. Inkjet printing of functional materials for optical and photonic applications. Materials. 2016;9(11):910.

[14] Alshammari AS, Alenezi MR, Lai KT, Silva SRP. Inkjet printing of polymer functionalized CNT gas sensor with enhanced sensing properties. Mater Lett. 2017;189:299–302.

[15] Liu X, Tarn T-J, Huang F, Fan J. Recent advances in inkjet printing synthesis of functional metal oxides. Particuology. 2015;19:1–13.

[16] Borghetti M, Serpelloni M, Sardini E, Pandini S. Mechanical behavior of strain sensors based on PEDOT:PSS and silver nanoparticles inks deposited on polymer substrate by inkjet printing. Sens Actuat A Phys. 2016;243:71–80.

[17] Matavž A, Malič B, Bobnar V. Inkjet printing of metal-oxide-based transparent thin-film capacitors. J Appl Phys. 2017;122(21):214102.

[18] Sharma S, Pande SS, Swaminathan P. Top-down synthesis of zinc oxide based inks for inkjet printing. RSC Adv. 2017;7(63):39411–9.

[19] Saunders RE, Derby B. Inkjet printing biomaterials for tissue engineering: bioprinting. Int Mater Rev. 2014;59(8):430–48.

[20] Tao H, Marelli B, Yang M, An B, Onses MS, Rogers JA, et al. Inkjet Printing of regenerated silk fibroin: from printable forms to printable functions. Adv Mater. 2015;27(29):4273–9.

[21] Xu H, Casillas J, Xu C. Effects of printing conditions on cell distribution within microspheres during inkjet-based bio-printing. AIP Adv. 2019;9(9):095055.

[22] Park J-U, Hardy M, Kang SJ, Barton K, Adair K, Mukhopadhyay DK, et al. High-resolution electrohydrodynamic jet printing. Nat Mater. 2007;6(10):782–9.

[23] Barton K, Mishra S, Alleyne A, Ferreira P, Rogers J. Control of high-resolution electrohydrodynamic jet printing. Control Eng Pract. 2011;19(11):1266–73.

[24] Lu Z, Peng Z, Liu C, Wang Z, Wang Y, Jiao X, et al. Current Status and Future Perspective of Immunotherapy in Gastrointestinal Cancers. The Innovation. 2020;1(2):100041.

[25] Lee K-H, Lee S-S, Ahn DB, Lee J, Byun D, Lee S-Y. Ultrahigh areal number density solid-state on-chip microsupercapacitors via electrohydrodynamic jet printing. Sci Adv. 2020;6(10):eaaz1692.

[26] Cho TH, Farjam N, Allemang CR, Pannier CP, Kazyak E, Huber C, et al. Area-selective atomic layer deposition patterned by electrohydrodynamic jet printing for additive manufacturing of functional materials and devices. ACS Nano. 2020;14(12):17262–72.

[27] Mkhize N, Murugappan K, Castell MR, Bhaskaran H. Electrohydrodynamic jet printed conducting polymer for enhanced chemiresistive gas sensors. J Mater Chem C. 2021;9(13):4591–6.

[28] Liu T, Huang R, Zhong J, Yang Y, Tan Z, Tan W. Control of cell proliferation in E-jet 3D-printed scaffolds for tissue engineering applications: the influence of the cell alignment angle. J Mater Chem B. 2017;5(20):3728–38.

[29] Vijayavenkataraman S, Zhang S, Lu WF, Fuh JYH. Electrohydrodynamic-jetting (EHD-jet) 3D-printed functionally graded scaffolds for tissue engineering applications. J Mater Res. 2018;33(14):1999–2011.

[30] Vijayavenkataraman S, Thaharah S, Zhang S, Lu WF, Fuh JYH. Electrohydrodynamic jet 3D-printed PCL/PAA conductive scaffolds with tunable biodegradability as nerve guide conduits (NGCs) for peripheral nerve injury repair. Mater Des. 2019;162:171–84.

[31] Xie C, Gao Q, Wang P, Shao L, Yuan H, Fu J, et al. Structure-induced cell growth by 3D printing of heterogeneous scaffolds with ultrafine fibers. Mater Des. 2019;181:108092.

[32] Sun J, Jing L, Liu H, Huang D. Generating nanotopography on PCL microfiber surface for better cell-scaffold interactions. Proc Manuf. 2020;48:619–24.

[33] Afkhami Z, Iezzi B, Hoelzle D, Shtein M, Barton KJ. Electrohydrodynamic jet printing of one-dimensional photonic crystals: part I–an empirical model for multi-material multi-layer fabrication. Adv Mater Technol. 2020;5(10):2000386.

[34] Can TTT, Nguyen TC, Choi W-SJ. High-viscosity copper paste patterning and application to thin-film transistors using electrohydrodynamic jet printing. Adv Eng Mater. 2020;22(3):1901384.

[35] Zou W, Yu H, Zhou P, Zhong Y, Wang Y, Liu LJ. High-resolution additive direct writing of metal micro/nanostructures by electrohydrodynamic jet printing. Appl Surf Sci. 2021;543:148800.

[36] Saba MH, Mukherjee S, Dutta S, Mallisetty PK, Murmu NC. Electrohydrodynamic jet printing for desired print diameter. Mater Today: Proc. 2021;46:1749–54.
[37] Barton K, Mishra S, Alex Shorter K, Alleyne A, Ferreira P, Rogers J. A desktop electrohydrodynamic jet printing system. Mechatronics. 2010;20(5):611–6.
[38] An S, Lee MW, Kim NY, Lee C, Al-Deyab SS, James SC, et al. Effect of viscosity, electrical conductivity, and surface tension on direct-current-pulsed drop-on-demand electrohydrodynamic printing frequency. Appl Phys Lett. 2014;105(21):214102.
[39] Bober DB, Chen C. Pulsating electrohydrodynamic cone-jets: from choked jet to oscillating cone. J Fluid Mech. 2011;689:552–63.
[40] Yeung K-W, Dong Y, Chen L, Tang C-Y, Law W-C, Tsui GC-P, et al. Printability of photo-sensitive nanocomposites using two-photon polymerization. Nanotechnol Rev. 2020;9(1):418–26.
[41] Collins RT, Sambath K, Harris MT, Basaran OA. Universal scaling laws for the disintegration of electrified drops. Proc Natl Acad Sci. 2013;110(13):4905.
[42] Pan Y, Zeng L. Simulation and validation of droplet generation process for revealing three design constraints in electrohydrodynamic jet printing. Micromachines. 2019;10(2):94.
[43] Han Y, Wei C, Dong J. Droplet formation and settlement of phase-change ink in high resolution electrohydrodynamic (EHD) 3D printing. J Manuf Process. 2015;20:485–91.
[44] Wu W, Yang X, Zhang B, Yin Z, Jia B. The study on electric field distribution and droplet trajectory during electrohydrodynamic jet printing. Microsyst Technol. 2020;27(7):2745–50.
[45] Liu L, Yang X, Zhang B, Yin Z, Zou H. Trajectory analysis of the charged droplet during electrohydrodynamic jet printing. Microsyst Technol. 2020;27(8):1–7.
[46] Jaworek A, Krupa AJ. Classification of the modes of EHD spraying. J Aerosol Sci. 1999;30(7):873–93.
[47] Furbank RJ, Morris JF. An experimental study of particle effects on drop formation. Phys Fluids. 2004;16(5):1777–90.
[48] Conroy DT, Matar OK, Craster RV, Papageorgiou DT. Breakup of an electrified viscous thread with charged surfactants. Phys Fluids. 2011;23(2):022103.
[49] Lee MW, Kim NY, Yoon SS. On pinchoff behavior of electrified droplets. J Aerosol Sci. 2013;57:114–24.
[50] Lee MW, An S, Kim NY, Seo JH, Huh J-Y, Kim HY, et al. Effects of pulsing frequency on characteristics of electrohydrodynamic inkjet using micro-Al and nano-Ag particles. Exp Therm Fluid Sci. 2013;46:103–10.
[51] Huo Y, Wang J, Zuo Z, Fan Y. Visualization of the evolution of charged droplet formation and jet transition in electrostatic atomization. Phys Fluids. 2015;27(11):114105.
[52] Guo L, Duan Y, Deng W, Guan Y, Huang Y, Yin Z. Charged satellite drop avoidance in electrohydrodynamic dripping. Micromachines. 2019;10(3):172.
[53] Collins RT, Harris M, Basaran O. Breakup of electrified jets. J Fluid Mech. 2007;588:75–129.
[54] Jaworek A, Krupa A. Jet and drops formation in electrohydrodynamic spraying of liquids. A systematic approach. Exp Fluids. 1999;27(1):43–52.
[55] Hartman RPA, Brunner DJ, Camelot DMA, Marijnissen JCM, Scarlett B. Electrohydrodynamic atomization in the cone–jet mode physical modeling of the liquid cone and jet. J Aerosol Sci. 1999;30(7):823–49.
[56] Chen CH, Saville DA, Aksay IA. Scaling laws for pulsed electrohydrodynamic drop formation. Appl Phys Lett. 2006;89(12):124103.
[57] Choi HK, Park J-U, Park OO, Ferreira PM, Georgiadis JG, Rogers JA. Scaling laws for jet pulsations associated with high-resolution electrohydrodynamic printing. Appl Phys Lett. 2008;92(12):123109.
[58] Higuera FJ, Ibáñez SE, Hijano AJ, Loscertales IG. Pulsating emission of droplets from an electrified meniscus. J Aerosol Sci. 2013;66:193–208.
[59] Scheideler WJ, Chen C-H. The minimum flow rate scaling of Taylor cone-jets issued from a nozzle. Appl Phys Lett. 2014;104(2):024103.
[60] Lee A, Jin H, Dang H-W, Choi K-H, Ahn KH. Optimization of experimental parameters to determine the jetting regimes in electrohydrodynamic printing. Langmuir. 2013;29(44):13630–9.
[61] Lee S-H, Nguyen XH, Ko HS. Study on droplet formation with surface tension for electrohydrodynamic inkjet nozzle. J Mech Sci Technol. 2012;26(5):1403–8.
[62] Mohammadi K, Movahhedy MR, Khodaygan S. A multiphysics model for analysis of droplet formation in electrohydrodynamic 3D printing process. J Aerosol Sci. 2019;135:72–85.
[63] Han Y, Wei C, Dong J. Super-resolution electrohydrodynamic (EHD) 3D printing of micro-structures using phase-change inks. Manuf Lett. 2014;2(4):96–9.
[64] Wei C, Dong J. Hybrid hierarchical fabrication of three-dimensional scaffolds. J Manuf Process. 2014;16(2):257–63.
[65] Jang S, Kim Y, Oh JH. Influence of processing conditions and material properties on electrohydrodynamic direct patterning of a polymer solution. J Electron Mater. 2016;45(4):2291–8.
[66] Wang K, Stark JPW. Direct fabrication of electrically functional microstructures by fully voltage-controlled electrohydrodynamic jet printing of silver nano-ink. Appl Phys A. 2010;99(4):763–6.
[67] An BW, Kim K, Lee H, Kim S-Y, Shim Y, Lee D-Y, et al. High-resolution printing of 3D structures using an electrohydrodynamic inkjet with multiple functional inks. Adv Mater. 2015;27(29):4322–8.
[68] He J, Xu F, Cao Y, Liu Y, Li D. Towards microscale electrohydrodynamic three-dimensional printing. J Phys D Appl Phys. 2016;49(5):055504.
[69] Zhang B, Seong B, Nguyen V, Byun D. 3D printing of high-resolution PLA-based structures by hybrid electrohydrodynamic and fused deposition modeling techniques. J Micromech Microeng. 2016;26(2):025015.
[70] Huang Y, Wang X, Duan Y, Bu N, Yin Z. Controllable self-organization of colloid microarrays based on finite length effects of electrospun ribbons. Soft Matter. 2012;8(32):8302–11.
[71] Bu N, Huang Y, Wang X, Yin Z. Continuously tunable and oriented nanofiber direct-written by mechano-electrospinning. Mater Manuf Process. 2012;27(12):1318–23.
[72] He J, Xu F, Cao Y, Liu Y, Li D, Jin Z. Electrohydrodynamic direct-writing lithography: an alternative maskless technique for microstructure fabrication. Appl Phys Lett. 2014;105(25):253109.

[73] Han Y, Dong J. Design, modeling and testing of integrated ring extractor for high resolution electrohydrodynamic (EHD) 3D printing. J Micromech Microeng. 2017;27(3):035005.
[74] Song CH, Back SY, Yu SI, Lee HJ, Kim BS, Yang NY, et al. Direct-patterning of porphyrin dot arrays and lines using electrohydrodynamic jet printing. J Nanosci Nanotechnol. 2012;12(1):475–80.
[75] Jang Y, Hartarto Tambunan I, Tak H, Dat Nguyen V, Kang T, Byun D. Non-contact printing of high aspect ratio Ag electrodes for polycrystalline silicone solar cell with electrohydrodynamic jet printing. Appl Phys Lett. 2013;102(12):123901.
[76] Wei C, Dong J. Direct fabrication of high-resolution three-dimensional polymeric scaffolds using electrohydrodynamic hot jet plotting. J Micromech Microeng. 2013;23(2):025017.
[77] Yuan X, Ba Z, Xiong Z. Fine droplet generation using tunable electrohydrodynamic pulsation. J Micromech Microeng. 2015;25(7):075028.
[78] Han Y, Dong J. High-resolution electrohydrodynamic (EHD) direct printing of molten metal. Proc Manuf. 2017;10:845–50.
[79] Park J, Park J-W, Nasrabadi AM, Hwang J. Methodology to set up nozzle-to-substrate gap for high resolution electrohydrodynamic jet printing. Appl Phys Lett. 2016;109(13):134104.
[80] Hassan Saba M, Mukherjee S, Dutta S, Kumar Mallisetty P, Chandra Murmu N. Electrohydrodynamic jet printing for desired print diameter. Mater Today: Proc. 2020;46:1749–54.
[81] Mishra S, Barton KL, Alleyne AG, Ferreira PM, Rogers JA. High-speed and drop-on-demand printing with a pulsed electrohydrodynamic jet. J Micromech Microeng. 2010;20(9):095026.
[82] Kim J, Oh H, Kim SS. Electrohydrodynamic drop-on-demand patterning in pulsed cone-jet mode at various frequencies. J Aerosol Sci. 2008;39(9):819–25.
[83] Xu L, Wang X, Lei T, Sun D, Lin L. Electrohydrodynamic deposition of polymeric droplets under low-frequency pulsation. Langmuir. 2011;27(10):6541–8.
[84] Lee MW, Kang DK, Kim NY, Kim HY, James SC, Yoon SS. A study of ejection modes for pulsed-DC electrohydrodynamic inkjet printing. J Aerosol Sci. 2012;46:1–6.
[85] Rahman K, Khan A, Nam NM, Choi KH, Kim D-S. Study of drop-on-demand printing through multi-step pulse voltage. Int J Precis Eng Manuf. 2011;12(4):663–9.
[86] Park J, Kim B, Kim S-Y, Hwang J. Prediction of drop-on-demand (DOD) pattern size in pulse voltage-applied electrohydrodynamic (EHD) jet printing of Ag colloid ink. Appl Phys A. 2014;117(4):2225–34.
[87] Kim B, Kim I, Joo SW, Lim G. Electrohydrodynamic repulsion of droplets falling on an insulating substrate in an electric field. Appl Phys Lett. 2009;95(20):204106.
[88] Nguyen VD, Byun D. Mechanism of electrohydrodynamic printing based on ac voltage without a nozzle electrode. Appl Phys Lett. 2009;94(17):173509.
[89] Yudistira HT, Nguyen VD, Dutta P, Byun D. Flight behavior of charged droplets in electrohydrodynamic inkjet printing. Appl Phys Lett. 2010;96(2):023503.
[90] Park J, Hwang J. Fabrication of a flexible Ag-grid transparent electrode using ac based electrohydrodynamic Jet printing. J Phys D: Appl Phys. 2014;47(40):405102.
[91] Wei C, Qin H, Ramírez-Iglesias NA, Chiu C-P, Lee Y-S, Dong J. High-resolution ac-pulse modulated electrohydrodynamic jet printing on highly insulating substrates. J Micromech Microeng. 2014;24(4):045010.
[92] Wei C, Qin H, Chiu C-P, Lee Y-S, Dong J. Drop-on-demand E-jet printing of continuous interconnects with AC-pulse modulation on highly insulating substrates. J Manuf Syst. 2015;37:505–10.
[93] Qin H, Wei C, Dong J, Lee Y-S. Direct printing and electrical characterization of conductive micro-silver tracks by alternating current-pulse modulated electrohydrodynamic jet printing. J Manuf Sci Eng. 2016;139(2):021008.
[94] Kim H, Song J, Chung J, Hong D. Onset condition of pulsating cone-jet mode of electrohydrodynamic jetting for plane, hole, and pin type electrodes. J Appl Phys. 2010;108(10):102804.
[95] Xu L, Sun D. Electrohydrodynamic printing under applied pole-type nozzle configuration. Appl Phys Lett. 2013;102(2):024101.
[96] Tse L, Barton K. Airflow assisted printhead for high-resolution electrohydrodynamic jet printing onto non-conductive and tilted surfaces. Appl Phys Lett. 2015;107(5):054103.
[97] Pan Y, Chen X, Zeng L, Huang Y, Yin Z. Fabrication and evaluation of a protruding Si-based printhead for electrohydrodynamic jet printing. J Micromech Microeng. 2017;27(12):125004.
[98] Kim Y, Jang S, Oh JH. High-resolution electrohydrodynamic printing of silver nanoparticle ink via commercial hypodermic needles. Appl Phys Lett. 2015;106(1):014103.
[99] Kim S-Y, Kim Y, Park J, Hwang J. Design and evaluation of single nozzle with a non-conductive tip for reducing applied voltage and pattern width in electrohydrodynamic jet printing (EHDP). J Micromech Microeng. 2010;20(5):055009.
[100] Zou W, Yu H, Zhou P, Liu L. Tip-assisted electrohydrodynamic jet printing for high-resolution microdroplet deposition. Mater Des. 2019;166:107609.
[101] Lee D-Y, Shin Y-S, Park S-E, Yu T-U, Hwang J. Electrohydrodynamic printing of silver nanoparticles by using a focused nanocolloid jet. Appl Phys Lett. 2007;90(8):081905.
[102] Choi J, Kim Y-J, Lee S, Son SU, Ko HS, Nguyen VD, et al. Drop-on-demand printing of conductive ink by electrostatic field induced inkjet head. Appl Phys Lett. 2008;93(19):193508.
[103] Lee S, An K, Son S, Choi J. Satellite/spray suppression in electrohydrodynamic printing with a gated head. Appl Phys Lett. 2013;103(13):133506.
[104] Zhang X, Kobayashi I, Uemura K, Nakajima M. Direct observation and characterization of the generation of organic solvent droplets with and without triglyceride oil by electrospraying. Colloids Surf A Physicochem Eng Asp. 2013;436:937–43.
[105] Tse L, Barton K. A field shaping printhead for high-resolution electrohydrodynamic jet printing onto non-conductive and uneven surfaces. Appl Phys Lett. 2014;104(14):143510.
[106] Lee J-S, Kim S-Y, Kim Y-J, Park J, Kim Y, Hwang J, et al. Design and evaluation of a silicon based multi-nozzle for addressable jetting using a controlled flow rate in electrohydrodynamic jet printing. Appl Phys Lett. 2008;93(24):243114.
[107] Khan A, Rahman K, Kim DS, Choi KH. Direct printing of copper conductive micro-tracks by multi-nozzle

electrohydrodynamic inkjet printing process. J Mater Process Technol. 2012;212(3):700–6.
[108] Wang D, Zhao X, Lin Y, Liang J, Ren T, Liu Z, et al. Nanoscale coaxial focused electrohydrodynamic jet printing. Nanoscale. 2018;10(21):9867–79.
[109] Zhao X, Wang D, Lin Y, Sun Y, Ren T, Liang J, et al. Numerical simulation of coaxial electrohydrodynamic jet and printing nanoscale structures. Microsyst Technol. 2019;25(12):4651–61.
[110] Li Z, Al-Milaji KN, Zhao H, Chen D-R. Ink bridge control in the electrohydrodynamic printing with a coaxial nozzle. J Manuf Process. 2020;60:418–25.
[111] Quang Tran SB, Byun D, Nguyen VD, Yudistira HT, Yu MJ, Lee KH, et al. Polymer-based electrospray device with multiple nozzles to minimize end effect phenomenon. J Electrost. 2010;68(2):138–44.
[112] Choi K-H, Rahman K, Khan A, Kim D-S. Cross-talk effect in electrostatic based capillary array nozzles. J Mech Sci Technol. 2011;25(12):3053–62.
[113] Khan A, Rahman K, Hyun M-T, Kim D-S, Choi K-H. Multi-nozzle electrohydrodynamic inkjet printing of silver colloidal solution for the fabrication of electrically functional microstructures. Appl Phys A. 2011;104(4):1113.
[114] Choi K-H, Khan A, Rahman K, Doh Y-H, Kim D-S, Kwan K-R. Effects of nozzles array configuration on cross-talk in multi-nozzle electrohydrodynamic inkjet printing head. J Electrost. 2011;69(4):380–7.
[115] Sutanto E, Shigeta K, Kim YK, Graf PG, Hoelzle DJ, Barton KL, et al. A multimaterial electrohydrodynamic jet (E-jet) printing system. J Micromech Microeng. 2012;22(4):045008.
[116] Pan Y, Huang Y, Guo L, Ding Y, Yin Z. Addressable multi-nozzle electrohydrodynamic jet printing with high consistency by multi-level voltage method. AIP Adv. 2015;5(4):047108.
[117] Kang DK, Lee MW, Kim HY, James SC, Yoon SS. Electrohydrodynamic pulsed-inkjet characteristics of various inks containing aluminum particles. J Aerosol Sci. 2011;42(10):621–30.
[118] Guo L, Duan Y, Huang Y, Yin Z. Experimental study of the influence of ink properties and process parameters on ejection volume in electrohydrodynamic jet printing. Micromachines. 2018;9(10):522.
[119] Kwon JO, Yang JS, Chae JB, Chung SK. Micro-object manipulation in a microfabricated channel using an electromagnetically driven microrobot with an acoustically oscillating bubble. Sens Actuat A Phys. 2014;215:77–82.
[120] Huang Y, Jiang L, Li B, Premaratne P, Jiang S, Qin H. Study effects of particle size in metal nanoink for electrohydrodynamic inkjet printing through analysis of droplet impact behaviors. J Manuf Process. 2020;56:1270–6.
[121] Bae J, Lee J, Hyun Kim S. Effects of polymer properties on jetting performance of electrohydrodynamic printing. J Appl Polym Sci. 2017;134(35):45044.
[122] Yu M, Ahn KH, Lee SJ. Design optimization of ink in electrohydrodynamic jet printing: effect of viscoelasticity on the formation of Taylor cone jet. Mater Des. 2016;89:109–15.
[123] Panahi A, Pishevar AR, Tavakoli MR. Experimental investigation of electrohydrodynamic modes in electrospraying of viscoelastic polymeric solutions. Phys Fluids. 2020;32(1):012116.
[124] Divvela MJ, Joo YL. Design principles in continuous inkjet electrohydrodynamic printing from discretized modeling and image analysis. J Manuf Process. 2020;54:413–9.
[125] Wang K, Paine MD, Stark JPW. Fully voltage-controlled electrohydrodynamic jet printing of conductive silver tracks with a sub-100 μm linewidth. J Appl Phys. 2009;106(2):024907.
[126] Kang J, Jang Y, Kim Y, Cho S-H, Suhr J, Hong BH, et al. An Ag-grid/graphene hybrid structure for large-scale, transparent, flexible heaters. Nanoscale. 2015;7(15):6567–73.
[127] Wang X, Xu L, Zheng G, Cheng W, Sun D. Pulsed electrohydrodynamic printing of conductive silver patterns on demand. Sci China Technol Sci. 2012;55(6):1603–7.
[128] Son S, Lee S, Choi J. Fine metal line patterning on hydrophilic non-conductive substrates based on electrohydrodynamic printing and laser sintering. J Electrost. 2014;72(1):70–5.
[129] Barnes TM, Reese MO, Bergeson JD, Larsen BA, Blackburn JL, Beard MC, et al. Comparing the fundamental physics and device performance of transparent, conductive nanostructured networks with conventional transparent conducting oxides. Adv Energy Mater. 2012;2(3):353–60.
[130] Lee H, Seong B, Kim J, Jang Y, Byun D. Direct alignment and patterning of silver nanowires by electrohydrodynamic jet printing. Small. 2014;10(19):3918–22.
[131] Seong B, Yoo H, Nguyen VD, Jang Y, Ryu C, Byun D. Metal-mesh based transparent electrode on a 3-D curved surface by electrohydrodynamic jet printing. J Micromech Microeng. 2014;24(9):097002.
[132] Schneider J, Rohner P, Thureja D, Schmid M, Galliker P, Poulikakos D. Electrohydrodynamic nanodrip printing of high aspect ratio metal grid transparent electrodes. Adv Funct Mater. 2016;26(6):833–40.
[133] Liu N, Zhang M, Yue T, Liu Y, Yang Y, Li WJ, et al. A microfluidic device with optically-controlled electrodes for on-demand electrical impedance measurement of targeted single cells. J Microelectromech Syst. 2020;29(6):1563–9.
[134] Jang Y, Kim J, Byun D. Invisible metal-grid transparent electrode prepared by electrohydrodynamic (EHD) jet printing. J Phys D: Appl Phys. 2013;46(15):155103.
[135] Wang K, Paine MD, Stark JPW. Freeform fabrication of metallic patterns by unforced electrohydrodynamic jet printing of organic silver ink. J Mater Sci: Mater Electron. 2009;20(11):1154–7.
[136] Jeong YJ, Bae J, Nam S, Lim S, Jang J, Kim SH, et al. Directly drawn ZnO semiconductors and MWCNT/PSS electrodes via electrohydrodynamic jet printing for use in thin-film transistors: the ideal combination for reliable device performances. Org Electron. 2016;39:272–8.
[137] Lee Y, Kim T-S, Min S-Y, Xu W, Jeong S-H, Seo H-K, et al. Individually position-addressable metal-nanofiber electrodes for large-area electronics. Adv Mater. 2014;26(47):8010–6.
[138] Li X, Kwon H-J, Qi X, Choi HK, Lim S, Kim T-W, et al. Direct-patterned copper/poly(ethylene oxide) composite electrodes for organic thin-film transistors through cone-jet mode by electrohydrodynamic jet printing. J Ind Eng Chem. 2020;85:269–75.
[139] Park SH, Kim J, Park CE, Lee J, Lee HS, Lim S, et al. Optimization of electrohydrodynamic-printed organic electrodes for bottom-contact organic thin film transistors. Org Electron. 2016;38:48–54.

[140] Lee YG, Choi W-S. Electrohydrodynamic jet-printed zinc–tin oxide tfts and their bias stability. ACS Appl Mater Interfaces. 2014;6(14):11167–72.
[141] Li X, Kim K, Oh H, Moon HC, Nam S, Kim SH. Cone-jet printing of aligned silver nanowire/poly(ethylene oxide) composite electrodes for organic thin-film transistors. Org Electron. 2019;69:190–9.
[142] Kwack Y-J, Choi W-S. Solution-processed zinc-tin-oxide thin-film transistor by electrohydrodynamic spray. Electron Mater Lett. 2012;8(3):341–4.
[143] Kim SY, Kim K, Hwang YH, Park J, Jang J, Nam Y, et al. High-resolution electrohydrodynamic inkjet printing of stretchable metal oxide semiconductor transistors with high performance. Nanoscale. 2016;8(39):17113–21.
[144] Kwack Y-J, Choi W-S. Patterning and passivation effects of zinc-tin-oxide thin-film transistors using an electrohydrodynamic jet printer. Mater Res Bull. 2019;114:170–6.
[145] Liu N, Lin Y, Peng Y, Xin L, Yue T, Liu Y, et al. Automated parallel electrical characterization of cells using optically-induced dielectrophoresis. IEEE Trans Autom Sci Eng. 2020;17(2):1084–92.
[146] Lee S, Kim J, Choi J, Park H, Ha J, Kim Y, et al. Patterned oxide semiconductor by electrohydrodynamic jet printing for transparent thin film transistors. Appl Phys Lett. 2012;100(10):102108.
[147] Pikul JH, Graf P, Mishra S, Barton K, Kim Y, Rogers JA, et al. High precision electrohydrodynamic printing of polymer onto microcantilever sensors. IEEE Sens J. 2011;11(10):2246–53.
[148] Corbin EA, Millet LJ, Pikul JH, Johnson CL, Georgiadis JG, King WP, et al. Micromechanical properties of hydrogels measured with MEMS resonant sensors. Biomed Microdevices. 2013;15(2):311–9.
[149] Muth JT, Vogt DM, Truby RL, Mengüç Y, Kolesky DB, Wood RJ, et al. Embedded 3D printing of strain sensors within highly stretchable elastomers. Adv Mater. 2014;26(36):6307–12.
[150] Huang Y, Ding Y, Bian J, Su Y, Zhou J, Duan Y, et al. Hyper-stretchable self-powered sensors based on electrohydrodynamically printed, self-similar piezoelectric nano/microfibers. Nano Energy. 2017;40:432–9.
[151] Choi KH, Zubair M, Dang HW. Characterization of flexible temperature sensor fabricated through drop-on-demand electrohydrodynamics patterning. Jpn J Appl Phys. 2014;53(5S3):05HB2.
[152] Ali S, Hassan A, Hassan G, Bae J, Lee CH. All-printed humidity sensor based on graphene/methyl-red composite with high sensitivity. Carbon. 2016;105:23–32.
[153] Zeeshan Yousaf HM, Kim SW, Hassan G, Karimov K, Choi KH, Sajid M. Highly sensitive wide range linear integrated temperature compensated humidity sensors fabricated using Electrohydrodynamic printing and electrospray deposition. Sens Actuat B Chem. 2020;308:127680.
[154] Qin H, Cai Y, Dong J, Lee Y-S. Direct printing of capacitive touch sensors on flexible substrates by additive E-jet printing with silver nanoinks. J Manuf Sci Eng. 2016;139(3):031011.
[155] Qin H, Dong J, Lee Y-S. Fabrication and electrical characterization of multi-layer capacitive touch sensors on flexible substrates by additive e-jet printing. J Manuf Process. 2017;28:479–85.
[156] Han Y, Dong J. Electrohydrodynamic (EHD) printing of molten metal ink for flexible and stretchable conductor with self-healing capability. Adv Mater Technol. 2018;3(3):1700268.
[157] Kang K, Yang D, Park J, Kim S, Cho I, Yang H-H, et al. Micropatterning of metal oxide nanofibers by electrohydrodynamic (EHD) printing towards highly integrated and multiplexed gas sensor applications. Sens Actuat B Chem. 2017;250:574–83.
[158] Wu H, Yu J, Cao R, Yang Y, Tang Z. Electrohydrodynamic inkjet printing of Pd loaded $SnO_2$ nanofibers on a CMOS micro hotplate for low power $H_2$ detection. AIP Adv. 2018;8(5):055307.
[159] Zhang B, Lee J, Kim M, Lee N, Lee H, Byun D. Direct patterning and spontaneous self-assembly of graphene oxide via electrohydrodynamic jet printing for energy storage and sensing. Micromachines. 2020;11:1.
[160] Kim MS, Kim G. Electrohydrodynamic jet process for pore-structure-controlled 3d fibrous architecture as a tissue regenerative material: fabrication and cellular activities. Langmuir. 2014;30(28):8551–7.
[161] Zhao X, He J, Xu F, Liu Y, Li D. Electrohydrodynamic printing: a potential tool for high-resolution hydrogel/cell patterning. Virtual Phys Prototyp. 2016;11(1):57–63.
[162] Zhang B, He J, Lei Q, Li D. Electrohydrodynamic printing of sub-microscale fibrous architectures with improved cell adhesion capacity. Virtual Phys Prototyp. 2020;15(1):62–74.
[163] Yang W, Chu H, Cai S, Liang W, Yu H, Wang Y, et al. Micropatterned cell-repellent interface using femtosecond laser direct writing to engineer controlled cell organization. Adv Mat Technol. 2021:2100178.
[164] Poellmann MJ, Barton KL, Mishra S, Johnson AJW. Patterned hydrogel substrates for cell culture with electrohydrodynamic jet printing. Macromol Biosci. 2011;11(9):1164–8.
[165] Poellmann MJ, Johnson AJW. Multimaterial polyacrylamide: fabrication with electrohydrodynamic jet printing, applications, and modeling. Biofabrication. 2014;6(3):035018.
[166] Wu Y, Sriram G, Fawzy AS, Fuh JYH, Rosa V, Cao T, et al. Fabrication and evaluation of electrohydrodynamic jet 3D printed polycaprolactone/chitosan cell carriers using human embryonic stem cell-derived fibroblasts. J Biomater Appl. 2016;31(2):181–92.
[167] Wang D, Jing L, Liu H, Huang D, Sun J. Microscale scaffolds with diverse morphology via electrohydrodynamic jetting for in vitro cell culture application. Biomed Phys Eng Express. 2019;5(2):025011.
[168] Jayasinghe SN, Qureshi AN, Eagles PAM. Electrohydrodynamic jet processing: an advanced electric-field-driven jetting phenomenon for processing living cells. Small. 2006;2(2):216–9.
[169] Townsend-Nicholson A, Jayasinghe SN. Cell electrospinning: a unique biotechnique for encapsulating living organisms for generating active biological microthreads/scaffolds. Biomacromolecules. 2006;7(12):3364–9.
[170] Kwok A, Arumuganathar S, Irvine S, McEwan JR, Jayasinghe SN. A hybrid bio-jetting approach for directly engineering living cells. Biomed Mater. 2008;3(2):025008.
[171] Umezu S, Ohmori H. Characteristics on micro-biofabrication by patterning with electrostatically injected droplet. CIRP Ann. 2014;63(1):221–4.
[172] Liaudanskaya V, Gasperini L, Maniglio D, Motta A, Migliaresi C. Assessing the impact of electrohydrodynamic jetting on encapsulated cell viability, proliferation, and ability to self-assemble in three-dimensional structures. Tissue Eng Part C Methods. 2014;21(6):631–8.

[173] Gasperini L, Maniglio D, Motta A, Migliaresi C. An electrohydrodynamic bioprinter for alginate hydrogels containing living cells. Tissue Eng Part C Methods. 2014;21(2):123–32.
[174] Wang J, Huang R, Chen H, Qiao X, Shi X, Wang X, et al. Personalized single-cell encapsulation using E-jet 3D printing with AC-pulsed modulation. Macromol Mater Eng. 2019;304(4):1800776.
[175] Li JL, Cai YL, Guo YL, Fuh JYH, Sun J, Hong GS, et al. Fabrication of three-dimensional porous scaffolds with controlled filament orientation and large pore size via an improved E-jetting technique. J Biomed Mater Res Part B Appl Biomater. 2014;102(4):651–8.
[176] Bas O, De-Juan-Pardo EM, Meinert C, D'Angella D, Baldwin JG, Bray LJ, et al. Biofabricated soft network composites for cartilage tissue engineering. Biofabrication. 2017;9(2):025014.
[177] Wu Y, Wang Z, Ying Hsi Fuh J, San Wong Y, Wang W, San, et al. Direct E-jet printing of three-dimensional fibrous scaffold for tendon tissue engineering. J Biomed Mater Res Part B Appl Biomater. 2017;105(3):616–27.
[178] Wu Y, Wu B, Vijayavenkataraman S, Wong YS, Fuh JYH. Crimped fiber with controllable patterns fabricated via electrohydrodynamic jet printing. Mater Des. 2017;131:384–93.
[179] Ahn SH, Lee HJ, Kim GH. Polycaprolactone scaffolds fabricated with an advanced electrohydrodynamic direct-printing method for bone tissue regeneration. Biomacromolecules. 2011;12(12):4256–63.
[180] Visser J, Melchels FPW, Jeon JE, van Bussel EM, Kimpton LS, Byrne HM, et al. Reinforcement of hydrogels using three-dimensionally printed microfibres. Nat Commun. 2015;6(1):6933.
[181] Qu X, Xia P, He J, Li D. Microscale electrohydrodynamic printing of biomimetic PCL/nHA composite scaffolds for bone tissue engineering. Mater Lett. 2016;185:554–7.
[182] Kim M, Yun H-S, Kim GH. Electric-field assisted 3D-fibrous bioceramic-based scaffolds for bone tissue regeneration: Fabrication, characterization, and in vitro cellular activities. Sci Rep. 2017;7(1):3166.
[183] Kim M, Yeo M, Kim M, Kim G. Biomimetic cellulose/calcium-deficient-hydroxyapatite composite scaffolds fabricated using an electric field for bone tissue engineering. RSC Adv. 2018;8(37):20637–47.
[184] Abbasi N, Abdal-hay A, Hamlet S, Graham E, Ivanovski S. Effects of Gradient and offset architectures on the mechanical and biological properties of 3-D melt electrowritten (MEW) scaffolds. ACS Biomater Sci Eng. 2019;5(7):3448–61.
[185] Lei Q, He J, Li D. Electrohydrodynamic 3D printing of layer-specifically oriented, multiscale conductive scaffolds for cardiac tissue engineering. Nanoscale. 2019;11(32):15195–205.
[186] Mao M, He J, Li Z, Han K, Li D. Multi-directional cellular alignment in 3D guided by electrohydrodynamically-printed microlattices. Acta Biomater. 2020;101:141–51.
[187] Altun E, Ekren N, Kuruca SE, Gunduz O. Cell studies on electrohydrodynamic (EHD)-3D-bioprinted bacterial cellulose \polycaprolactone scaffolds for tissue engineering. Mater Lett. 2019;234:163–7.
[188] Wu B, Wu Y, Lu WF, Fuh JYH. Polycaprolactone/pluronic F127 tissue engineering scaffolds via electrohydrodynamic jetting for gastro intestinal repair. Proc CIRP. 2017;65:184–8.
[189] He J, Xu F, Dong R, Guo B, Li D. Electrohydrodynamic 3D printing of microscale poly ($\varepsilon$-caprolactone) scaffolds with multi-walled carbon nanotubes. Biofabrication. 2017;9(1):015007.
[190] Meng Z, He J, Xia Z, Li D. Fabrication of microfibrous PCL/MWCNTs scaffolds via melt-based electrohydrodynamic printing. Mater Lett. 2020;278:128440.
[191] Bai J, Wang H, Gao W, Liang F, Wang Z, Zhou Y, et al. Melt electrohydrodynamic 3D printed poly ($\varepsilon$-caprolactone)/polyethylene glycol/roxithromycin scaffold as a potential anti-infective implant in bone repair. Int J Pharm. 2020;576:118941.
[192] Jiang L, Huang Y, Zhang X, Qin H. Electrohydrodynamic inkjet printing of Polydimethylsiloxane (PDMS). Procedia Manuf. 2020;48:90–4.
[193] Chen M, Lee H, Yang J, Xu Z, Huang N, Chan BP, et al. Parallel, multi-material electrohydrodynamic 3D nanoprinting. Small. 2020;16(13):1906402.
[194] Park HG, Byun SU, Jeong HC, Lee JW, Seo DS. Photoreactive spacer prepared using electrohydrodynamic printing for application in a liquid crystal device. ECS Solid State Lett. 2013;2(12):R52–4.
[195] Park S-E, Kim S, Lee D-Y, Kim E, Hwang J. Fabrication of silver nanowire transparent electrodes using electrohydrodynamic spray deposition for flexible organic solar cells. J Mater Chem A. 2013;1(45):14286–93.
[196] Liang Y, Yong J, Yu Y, Nirmalathas A, Ganesan K, Evans R, et al. Direct electrohydrodynamic patterning of high-performance all metal oxide thin-film electronics. ACS Nano. 2019;13(12):13957–64.
[197] Kwon H-j LiX, Hong J, Park CE, Jeong YJ, Moon HC, et al. Non-lithographic direct patterning of carbon nanomaterial electrodes via electrohydrodynamic-printed wettability patterns by polymer brush for fabrication of organic field-effect transistor. Appl Surf Sci. 2020;515:145989.
[198] Rasekh M, Ahmad Z, Day R, Wickam A, Edirisinghe M. Direct writing of polycaprolactone polymer for potential biomedical engineering applications. Adv Eng Mater. 2011;13(9):B296–305.
[199] Shigeta K, He Y, Sutanto E, Kang S, Le A-P, Nuzzo RG, et al. Functional protein microarrays by electrohydrodynamic jet printing. Anal Chem. 2012;84(22):10012–8.